Computational studies of semiconductor quantum dots

Olli Lehtonen, Dage Sundholm* and Tommy Vänskä

Received 11th March 2008, Accepted 16th June 2008
First published as an Advance Article on the web 9th July 2008
DOI: 10.1039/b804212h

Light-absorption and luminescence processes in nano-sized materials can be modelled either by using computational approaches developed for quantum chemical calculations or by applying computational methods in the effective mass approximation (EMA) originally intended for solid-state theory studies. An overview of the theory and implementation of an *ab initio* correlation EMA method for studies of luminescence properties of embedded semiconductor quantum dots is presented. The applicability of the method and the importance of correlation effects are demonstrated by calculations on InGaAs/GaAs quantum-dot and quantum-ring samples. *Ab initio* and density functional theory (DFT) quantum chemical studies of optical transitions in freestanding silicon nanoclusters are also discussed. The accuracy of the optical gaps and oscillator strengths for silicon nanoclusters obtained using different computational methods is addressed. Changes in the cluster structures, excitation energies and band strengths upon excitation are reported. The role of the surface termination and functional groups on the silicon nanocluster surfaces is discussed.

I. Introduction

Semiconductor quantum dots can largely be divided into two main classes, namely freestanding and embedded quantum dots. Clusters and nanocrystals consisting of one kind of atoms or of molecular compounds as well as large molecules can be considered to belong to the first category.[1,2] In the synthesis, dangling bonds at the surface of the freestanding quantum dot can be terminated with hydrogen or larger ligating groups.[3–5] The embedded quantum dots are self-assembled structures fused and integrated into a surrounding matrix[6–9] or manufactured by lithography and chemical etching.[10] Embedded quantum dots can be considered as some kind of defect in the solid-state material perturbing the periodicity of the bulk structure[11] suggesting the use of models based on the effective-mass approximation (EMA) in quantum-dot studies.[12] The two categories of quantum dots are in general studied computationally by using different computational approaches.[2,8,12–18] Computational methods developed for molecular electronic structure calculation are used in studies on freestanding quantum dots,[2,14,16,18,19–23] whereas computational methods employing EMA models originally intended for calculations on bulk materials are the standard approach in studies on embedded quantum dots.[8,12,13,24] Large freestanding quantum dots have also been studied computationally using EMA approaches.[25–27] However, for freestanding quantum dots it is not trivial to determine the effective confinement potential from basic principles. The use of particle-in-a-box-like confinement potentials gives a taste of semi-empirical character of the EMA approach in studies on freestanding quantum dots.[28,29] Such simple EMA models tend to exaggerate the confinement effects,[30,31] whereas improved EMA models with nonspherical confinement potentials yield energies in slightly better agreement with experiment.[32–35] A qualitative explanation of the confinement energy effects and the dependence of the strength of the photoluminescence with respect to the cluster size can be obtained using EMA calculations on freestanding quantum dots.[36,37] For embedded quantum-dots rather accurate

Department of Chemistry, University of Helsinki, P.O. Box 55 (A.I. Virtasen Aukio 1), FIN-00014, Finland.
E-mail: olehtone@chem.helsinki.fi; sundholm@chem.helsinki.fi; tommy@chem.helsinki.fi

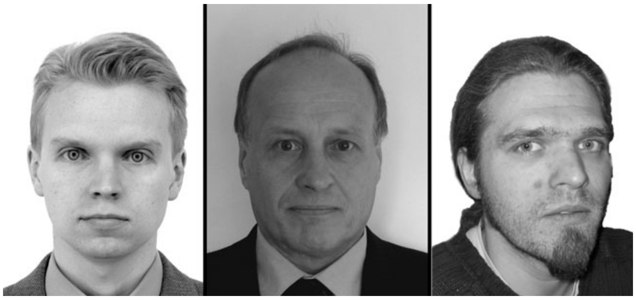

Olli Lehtonen studied materials physics at the Helsinki University of Technology and obtained his DSc degree in 2007. He is currently working as a post-doctoral researcher at the University of Helsinki. His research interests are theoretical and computational nanoscience.

Dage Sundholm is a senior research scientist at the University of Helsinki, where he holds a docentship in physical chemistry. His research interests are numerical quantum chemistry methods as well as computational studies of optical and magnetic properties of molecules and nanosystems.

Tommy Vänskä studied material physics at the Helsinki University of Technology. He is currently a doctoral student at the University of Helsinki. His research interest is development of computational methods for nanostructure studies.

confinement potentials can be obtained using strain calculations.[6] Atomistic methods for computational studies of embedded quantum dots have also been developed.[2,38]

The molecular and EMA approaches have their own pros and cons and are complementary. EMA calculations have difficulties to accurately describe processes in very small quantum dots because the microscopic structure at the atomic level determines their optical properties. The strength of the EMA approach is its ability to describe large quantum dots for which mainly the confinement effects influence their properties. The transition from large quantum dots to bulk material can be made smoothly at the EMA level by using systematically larger and shallower confinement potentials. Molecular approaches are preferable for small quantum dots regardless of whether they are freestanding or embedded in a matrix.

The EMA equations for semiconductor quantum dots containing many particles are often solved using rather unsophisticated computational methods, because the rough approximations of the EMA model are assumed to limit the accuracy anyhow. The discrepancies between calculated and experimental data can thus be due to the EMA approximation or due to the employed computational methods. Excitonic systems involving one electron-hole pair can be modelled using exact diagonalization approaches corresponding to full configuration interaction.[8] For many-particle quantum dots, the construction and diagonalization of the full Hamiltonian matrix become computationally expensive. In semiconductor quantum-dot studies aiming at high accuracy, correlation effects have to be considered because the formally opposite charge of the electrons and the holes renders correlation important for luminescence processes.

The EMA and the atomistic approaches are both useful when aiming at a deeper understanding of the photoluminescence (PL) properties of semiconductor quantum dots. Molecular electronic structure calculations at density functional theory (DFT) levels are limited to molecules consisting of up to a few thousands of atoms. The applicability of DFT calculations will though in a near future be extended to much larger systems.[39–44]

The approximate density functionals of today are not perfect implying that DFT results must be assessed by comparing them to accurate values obtained at *ab initio* levels of theory or to unambiguous experimental data. Such comparisons yield the magnitude and sources of errors of the DFT calculations. Accurate estimates for excitation energies can be obtained by adjusting the DFT values using correction factors obtained in benchmark studies. The benchmark calculations are performed on smaller species because highly correlated *ab initio* calculations are not feasible for very large systems. The coupled-cluster approximate singles and doubles (CC2) model is currently the most advanced correlated *ab initio* approach feasible for studies of quantum dots.[23,45] The number of amplitudes describing the left and right CC2 wave functions is the same as the number of coefficients parameterising an excited state at the time-dependent DFT (TDDFT) level. The computational effort to determine the amplitudes is though significantly larger than for solving the linear response equations of the TDDFT method. The basis set convergence is also slower for *ab initio* approaches than for DFT based methods. CC2 calculations are today applicable on medium-size molecules[46,47] and small quantum dots.[17,48]

The DFT and *ab initio* approaches that can be employed in studies of large molecules cannot accurately describe multiply excited states, because neither the linear response DFT (TDDFT) method using today's approximate functionals, nor the linear response CC2 method, are able to provide accurate excited states with significant multiple excitation character. In semiconductor quantum-dot studies, this implies that properties of multiexciton complexes are hard to calculate accurately using the linear response methods. In EMA calculations, the difference between excitons and multiexcitonic complexes appears as the number of quasi particles to be considered in the calculation. Calculations on exciton systems are two-body correlation problems involving one electron–hole pair, whereas calculations on multiexcitonic complexes are more complicated because interactions between several electrons and holes must be considered in the many-body calculation.

In this work, we present a overview of our computational studies on freestanding silicon quantum dots using DFT and CC2 methods aimed for molecular electronic structure calculations. The properties of the excited states and the transition probabilities between the ground state and the excited states are calculated using the corresponding linear response formalism. The employed TDDFT and CC2 linear response methods are not thoroughly discussed here because they have been developed and implemented by other researchers.[21,23] The EMA method for studies of semiconductor quantum dots is instead presented in more detail, because a two-band EMA approach considering electron-hole correlation effects has been developed and implemented by us and coworkers.[13,49–58] The applicability of the EMA approach on embedded quantum dots is demonstrated by calculations on a strain-induced InGaAs/GaAs quantum-dot sample as well as on quantum-dot and quantum-ring models using the same material parameters.

II. Freestanding silicon quantum dots

Crystalline silicon is known to be a poor light emitter due to its indirect optical band gap.[59] Research activities in semiconductor optoelectronics were originally focused on compound semiconductors[59] with direct band gaps, thus enabling efficient light emission. Porous silicon was found to be photoluminescent at cryogenic temperatures in the mid-80s,[60] but when Canham *et al.*[61] discovered that silicon nanostructures are photoluminescent at room temperature, it became apparent that silicon can be useful in optical applications and devices.[62] Strong PL from porous silicon occurs in the energy range of red to yellow light, whereas the blue emission is rather weak.[63] Freestanding silicon nanoclusters were synthesised later on and found to be light emitters with strong luminescence in the energy range from red to blue depending on their size.[1,64–66]

The origin of the PL is not understood and no consensus prevails concerning the PL mechanism at the atomic level. Different mechanisms for the light emission from porous silicon have been proposed. These comprise quantum confinement effects, nanocrystal surface states, defects, molecular functional groups, and structural disorder.[66–68] It has even been proposed that the observed light would be due to thermal radiation.[69] The most popular explanation of the bright luminescence is quantum confinement.

The exciton generated by an applied laser field is confined inside the nanocrystals in porous silicon and the emitted light is created through radiative recombination processes of the electron–hole pair. In crystalline silicon and other semiconductors with indirect band gaps, the optical recombination transition is forbidden, unless lattice vibrations (phonons) are involved in order to conserve crystal momentum. The spatial confinement of electrons and holes inside nanocrystals increases the uncertainty of the crystal momentum and optical transitions become allowed.[70] For a narrow confinement potential, the PL energy is larger than for a flat one, analogous to the solutions of the Schrödinger equation for a particle in a box. According to the quantum-confinement model, the recombination rate of electrons and holes increases with decreasing size of the cluster. The quantum-confinement model has proven to be very successful to predicting PL properties in good agreement with observations, at least as far as the energy of the emitted light is concerned.

The confinement model provides limited information about the emission mechanism at the atomic level. Hitherto, little is known about the luminescence mechanism and the microscopic nature of the quantum-dot structure at the light-emission centres. Besides the cluster size, there are other factors that affect the optical properties of the silicon nanoclusters because all silicon nanoclusters are not strongly luminescent.[71] The shape and crystal structure might be important, but the surface chemistry including active functional groups at the cluster surface certainly influences the optical properties of silicon nanoclusters. Computational studies of absorption and emission spectra of freestanding silicon nanoclusters show that the confinement model alone cannot explain the observed strong PL of silicon nanoclusters,[72] because the calculated band strengths for the hydrogen capped silicon nanoclusters[17,45,48,73] are several orders of magnitude smaller than obtained in the PL experiments.[74]

In preparative chemistry, new routes to synthesise silicon nanoclusters have been developed and also new approaches to tailor the surface chemistry are being evolved.[1,75] Strongly luminescent silicon nanoclusters with an optical yield exceeding 60% were recently synthesised.[76] The bright silicon nanoclusters were obtained by attaching octadecacene groups to their surface. In technical applications and for the microelectronic industry an interesting research direction is the design and construction of strongly luminescent silicon nanoclusters embedded in amorphous SiO_2 or in other transparent and robust matrices protecting the light emitters.[77] Polysilylenes also show promise as materials for strong luminescence and electroluminescence with applications in light-emitting diodes and flat-panel screens.[75,78,79]

III. Electronic spectra, oscillator strengths and lifetimes

A Absorption and emission processes

A more thorough understanding of the light-absorption and light-emission processes requires information about the potential-energy surfaces of both the ground and the involved excited states. The absorption of a photon excites the cluster in the ground state with its equilibrium geometry to an excited state. During the excitation process, the molecular structure is largely unchanged. However, the ground-state structure is not optimal for the excited state, resulting in a relaxation of the molecular structure of the excited state. The de-excitation giving rise to the luminescence can also be considered to occur vertically from the relaxed excited state structure. The optimised molecular structure of the excited state is not optimal for the ground state either. The ground-state energy for the excited state structure is somewhat higher in energy than for the ground-state geometry resulting in a redshift of the emitted light. The relaxation of the excited-state structure and the strain of the ground-state structure contribute to the Stokes shift.

Calculation of luminescence properties is much more involved than computing the electronic absorption spectrum. In accurate simulations of the luminescence, a variety of relaxation processes have to be considered because the observed light emission is the outcome of several competing and coupled processes. The emission intensity and the energy of the emitted light depend on the de-excitation route and populations of the levels. Both radiative and nonradiative processes have to be considered. The luminescence strength is obtained by solving the rate equations for the involved relaxation pathways. However, Stokes shifts and luminescence intensities can be estimated by comparing excitation energies and oscillator strengths calculated for the molecular structures of the ground and involved excited states, respectively. The difference between absorption and emission spectra is then assumed to be merely a consequence of the changes in the molecular structure.

Stimulated emission and optical gain necessary for laser action can be observed when population inversions between the ground and a radiating excited state occurs. Optical gain was recorded for the first time in embedded silicon nanoclusters by Pavesi *et al.*[77] They proposed a three-level model for the optical gain mechanism with a population inversion for a radiative state at the silicon nanocluster/silicon dioxide interface. The radiative state responsible for the optical gain lies energetically between the ground state and the absorbing excited states. The prerequisites for a silicon nanocluster based laser is strong absorption of light, a fast relaxation of the excited state, and an electron-hole recombination with a smaller transition probability from the relaxed excited state than for the absorption process.[62,76,77]

B Absorption and luminescence spectra

Simulated absorption spectra can be obtained from calculated excitation energies and oscillator strengths as

$$I_i(\omega) = \sum_{j=1}^{n} f_{ij} \frac{(\Omega/2)^2}{(\omega - \omega_{ij})^2 + (\Omega/2)^2}, \tag{3.1}$$

where ω_{ij} are excitation energies from state ψ_i, and f_{ij} are the corresponding oscillator strengths. The summation runs over all excited states ψ_j in the considered energy range. A Lorentzian line shape function with a line width (Ω) of 50 meV has been used in this work. The oscillator strengths f_{ij} for the light absorption process from a specific state ψ_i to all degenerate states of the upper level ψ_j is calculated as

$$f_{ij} = \frac{2}{3}\frac{\Delta E_{ij}}{g_i}S_{ij}^2 \tag{3.2}$$

where ΔE_{ij} is the excitation energy, g_i is the degeneration of ψ_i, and S_{ij}^2 is the squared transition moment calculated as

$$S_{ij}^2 = |\langle\psi_i|x|\psi_j\rangle|^2 + |\langle\psi_i|y|\psi_j\rangle|^2 + |\langle\psi_i|z|\psi_j\rangle|^2 \tag{3.3}$$

The expression for the oscillator strength in SI units is

$$f_{ij} = \frac{8\pi^2 m_e c a_0^2}{3h}\frac{\Delta E_{ij} S_{ij}^2}{g_i}, \tag{3.4}$$

where m_e is the electron mass, c is the speed of light in vacuum and a_0 is the Bohr radius. Inserting the latest values of the fundamental physical constants yields a working equation for the oscillator strength

$$f_{ij} = \frac{3.0375568 \times 10^{-6}}{g_i}\left[\frac{\Delta E_{ij}}{\mathrm{cm}^{-1}}\right]\left[\frac{S_{ij}^2}{\mathrm{a.u.}}\right] \tag{3.5}$$

The band strengths for comparison with experimental absorption spectra are obtained by multiplying the oscillator strength in eqn (3.5) by the state degeneration factors g_i and g_j. The luminescence intensity from state ψ_j is proportional to the de-excitation energy ΔE_{ji}, the degeneration of the upper level g_j, and the transition probability A_{ji} from the non-degenerate ψ_j state to all states of the lower level ψ_i.

$$I_{ji} \propto \Delta E_{ji} g_j A_{ji} \tag{3.6}$$

A_{ji} (in SI units) is given by

$$A_{ji} = \frac{16\pi^3 e^2 a_0^2}{3h\varepsilon_0}\frac{\Delta E_{ji}^3}{g_j} = \frac{2\pi e^2}{\varepsilon_0 m_e c}\frac{\Delta E_{ji}^2 g_i f_{ji}}{g_j}, \tag{3.7}$$

where h is the Planck constant, e is the elementary charge and ε_0 is the electric constant. The working equation for the transition probability then becomes

$$\left[\frac{A_{ji}}{s^{-1}}\right] = 0.66702517\left[\frac{\Delta E_{ji}}{\mathrm{cm}^{-1}}\right]^2\frac{g_i}{g_j}f_{ji} \tag{3.8}$$

The lifetime τ_{ji} of the excited state can be calculated as the inverse of the transition probability rate, when no other relaxation paths compete with the luminescence process. The working equation for the lifetime then reads

$$\left[\frac{\tau_{ji}}{s}\right] = 1.4991938\frac{g_j}{g_i}\frac{1}{f_{ji}}\left[\frac{\mathrm{cm}^{-1}}{\Delta E_{ji}}\right]^2 \tag{3.9}$$

C Luminescence in the EMA picture

In the EMA model, the electronic excitation from the filled valence band to the empty conduction band is expressed as the creation of an electron-hole pair. The de-excitation corresponds to recombination and annihilation of the carrier pair. In the recombination process, the energy is conserved by emission of a photon. In a semiconductor with embedded quantum dots, the excitation process occurs mainly in the bulk of semiconductor. After the excitation, the carrier pair moves along the valence and conduction bands towards the quantum dot where they are trapped by the attractive confinement potential forming an exciton. The recombination process of the carrier pair occurs in the quantum dot, because there the electrons and holes are spatially close to each other. The annihilation probability of the exciton is largely proportional to the overlap of the electron and hole orbitals of the exciton wave function. The luminescence energy depends on the semiconductor band gap and the energy levels of the exciton trapped in the quantum dot. The luminescence energy equals the exciton energy calculated using the EMA method plus the experimental band gap. The EMA computational methods are described in section IV.

In strong laser fields, the creation of the carrier pairs might be faster than the exciton annihilation in the quantum dot. Many electron-hole pairs are simultaneously trapped in the quantum dot; multiexciton complexes are formed. The energy levels of the multiexcitons can be obtained by solving the Schrödinger equation for interacting electrons and holes trapped by the confinement potential of the quantum dot. Doped quantum-dot samples might have a net positive or negative charge. The excess electrons or holes interacting with the carrier pairs of the excitons must then be considered in the calculation. The energy levels of the excitons in the quantum dot depend on the number of electrons and holes in the dot as well as the shape and size of the confinement potential. For example, a biexciton is bound when its energy is lower than the energy of two noninteracting excitons. When carrier pairs enter the dot, they emit excess energy to the surrounding semiconductor matrix as lattice vibrations (phonon). In the phonon-relaxation process, the exciton might be trapped and recombine in an excited state. This is called phonon bottleneck giving rise to extra peaks in the luminescence spectrum. The main nonradiative relaxation mechanisms of the excitons in the quantum dot are phonon relaxation and Auger recombination. In the Auger recombination of carrier pairs the energy is transferred to a third charge carrier exciting it to a higher energy state. The Auger process is a very important nonradiative recombination mechanism for freestanding quantum dots.[80,81]

IV. The effective-mass approximation

In the effective mass approximation (EMA), the wave functions $\Psi_n(\mathbf{r})$ for each band of the quantum-dot heterostructure are expressed as a product of a periodic Bloch function $u_{n,\mathbf{k}}(\mathbf{r})$ times an envelope function $\psi_n(\mathbf{r})$.[82]

$$\Psi_n(\mathbf{r}) = \psi_n(\mathbf{r})\exp(i\mathbf{k}\cdot\mathbf{r})u_{n,\mathbf{k}}(\mathbf{r}) \tag{4.10}$$

$u_{n,\mathbf{k}}(\mathbf{r})$ have a periodicity of the crystal (Bravais) lattice and the envelope functions $\psi_n(\mathbf{r})$ are determined by fulfilling the effective-mass Schrödinger equation. The envelope functions consider localised deviations from the wave function of the solid-state material. The EMA ansatz inserted into the Schrödinger equation yields an effective Hamiltonian where the bulk properties appear as an effective-mass tensor for each band.[8,12,83] The Coulomb interaction between the charge carriers are considered to be screened by the dielectric constant of the bulk semiconductor. The eigenvalues of the effective-mass Hamiltonian equal the deviation of the excitation energies from the band gap of the infinite crystal.

The number of bands considered in the EMA calculations on semiconductor quantum dots is two or more. The most popular EMA model is the **k**·**p** model which takes typically eight bands into account.[84] However, the two-band EMA model has mainly been applied in studies of multiexcitons and charged excitons at *ab initio* correlated levels,[8] especially when the energy splitting between the valence bands is large. The valence-band structure of GaAs-type semiconductors consists of heavy-hole (HH), light-hole (LH), and split-off bands. These bands arise from the spin–orbit (SO) coupling of the electron spin with the Coulomb field of the nucleus due to the orbital motion of the electron. Similar to isolated atoms, where SO coupling leads to the splitting of certain degenerate energy levels, in solids SO coupling leads to the splitting of the degenerate valence band states. The terms heavy and light hole arise from the different effective masses of the valence bands and the split-off hole is the band which is shifted in energy due to the SO coupling.

In the studied InGaAs/GaAs quantum-dot sample, the HH and LH bands are relatively well separated. They can therefore be treated independently resulting in the commonly used two-band effective-mass equation considering the electrons and the heavy holes.[8] The light-hole effects can be estimated by taking the HH–LH coupling into account at the perturbation theory level.[56]

A The two-band EMA Hamiltonian

The two-band effective-mass (Luttinger–Kohn) Hamiltonian is written as[8,53]

$$\hat{H} = \sum_{ij\sigma} h^{\mathrm{e}}_{ij} c^{\dagger}_{i,\sigma} c_{j,\sigma} + \sum_{rs\sigma} h^{\mathrm{h}}_{rs} d^{\dagger}_{r,\sigma} d_{s,\sigma} + \frac{1}{2} \sum_{ijkl\sigma\sigma'} g^{\mathrm{ee}}_{ijkl} c^{\dagger}_{i,\sigma} c^{\dagger}_{k,\sigma'} c_{l,\sigma'} c_{j,\sigma} + \frac{1}{2} \sum_{rstu\sigma\sigma'} g^{\mathrm{hh}}_{rstu} d^{\dagger}_{r,\sigma} d^{\dagger}_{t,\sigma'} d_{u,\sigma'} d_{s,\sigma} - \sum_{ijrs\sigma\sigma'} g^{\mathrm{eh}}_{ijrs} c^{\dagger}_{i,\sigma} c_{j,\sigma} d^{\dagger}_{r,\sigma'} d_{s,\sigma'}, \tag{4.11}$$

where $c^{\dagger}_{i,\sigma}$ creates an electron in the single-particle orbital *i* and $d^{\dagger}_{r,\sigma}$ creates a hole in *r*. The corresponding annihilation operators are $c_{i,\sigma}$ and $d_{r,\sigma}$. The two pseudospinor components, σ, can take the symbolic values of spin-up (↑) and spin-down (↓). The one-body electron and hole interaction terms, h^{e}_{ij} and h^{h}_{rs}, consist of the kinetic energy contribution and the interactions of the electrons and the holes with the confinement potentials $U^{\mathrm{e,h}}_{\mathrm{conf}}$.

$$h^{\mathrm{e}}_{ij} = \int \mathrm{d}\mathbf{x} \phi^{*}_{i}(\mathbf{x}) \left(\frac{\hat{p}^2_x}{2m^{\mathrm{e}}_x} + \frac{\hat{p}^2_y}{2m^{\mathrm{e}}_y} + \frac{\hat{p}^2_z}{2m^{\mathrm{e}}_z} + U^{\mathrm{e}}_{\mathrm{conf}} \right) \phi_j(\mathbf{x}). \tag{4.12}$$

Table 1 The material parameters for GaAs used in the EMA calculations. m^{e} is the effective electron mass ($m^{\mathrm{e}}_x = m^{\mathrm{e}}_y = m^{\mathrm{e}}_z$), m^{h} is the effective hole mass ($m_x = m_y$), m is the bare electron mass, ε_{r} is the relative dielectric constant, n is the refractive index, E_p is the Kane matrix element, D^{e} and D^{h} are deformation potentials of the electrons and the holes, v is the speed of sound, and ρ is the density of the semiconductor

m^{e}	m^{h}_{xy}	m^{h}_{z}	ε_{r}	n	E_p/eV	D^{e}/eV	D^{h}/eV	v/m s^{-1}	ρ/kg m^{-3}
0.0665m	0.143m	0.341m	13	3.6	25.7	8.6	6.7	3700	5300

The integration is done over $\mathbf{x} = \mathbf{r}$, σ. $\hat{p}$ is the momentum operator, m^{e}_x, m^{e}_y, and m^{e}_z are the diagonal elements of the effective-mass tensor for the electrons and $\phi_i(\mathbf{x})$ are the spin orbitals of the electrons. An analogous expression defines the one-body hole interaction integrals h^{h}_{rs}. The two-body Coulomb interaction terms g_{abcd} are given by

$$g_{abcd} = \int \mathrm{d}\mathbf{x}\mathrm{d}\mathbf{x}' \phi^{*}_{a}(\mathbf{x}) \phi^{*}_{c}(\mathbf{x}') \frac{1}{4\pi\varepsilon|\mathbf{r} - \mathbf{r}'|} \phi_b(\mathbf{x}) \phi_d(\mathbf{x}') \tag{4.13}$$

where ε is the dielectric constant of the semiconductor ($\varepsilon = \varepsilon_{\mathrm{r}}\varepsilon_0$). The hole and the electrons are considered as separate particles because of the wide bandgap. The Hamiltonian contains therefore no exchange interaction terms between the electrons and the holes. Electron-hole exchange interactions can though be taken into account by an *ad hoc* addition of Hamiltonian terms that are proportional to the overlap of the electron and the hole orbitals.[85,86]

The properties of the semiconductor quantum dots can be obtained by solving the Schrödinger equation for the Hamiltonian in eqn (4.11). For excitons, the wave function can be obtained by constructing the full Hamiltonian matrix and solving the eigenvalue problem by using exact diagonalization.[8] This is not a practical route for full configuration-interaction (CI) studies of multiexcitons. We have developed and implemented similar *ab initio* methods for solution of the EMA equations for semiconductor quantum dots as used in modern quantum chemical calculations. The electron–electron, hole–hole, and electron–hole correlation effects are considered at the CI[13,49–52,58] and general coupled-cluster (CC) levels.[57] In the quantum-dot CI and CC programs, the electrons and the holes are treated equally (Table 1).

B Phonon relaxation

The multiexciton system can lose its energy either through radiative[53] or nonradiative processes.[55] Multiexciton complexes can relax nonradiatively from an upper excited state in the quasi-particle picture to a lower excited state or to the ground state by emitting phonons to the surrounding semiconductor lattice. The phonon relaxation process involves initial ($\mathscr{R}$) and final ($\mathscr{L}$) states with equal number of electron-holes pairs. The Hamiltonian for the deformation-potential interactions between the longitudinal acoustical (LA) phonons of the lattice and the excitons can be expressed as[53,87]

$$\hat{H}_{\mathrm{LA}} = \sum_{ij} \sum_{\mathbf{q}} \langle i | w^{e}(\mathbf{q}) | j \rangle c^{\dagger}_{i} c_{j} (b^{\dagger}_{\mathbf{q}} + b_{-\mathbf{q}}) + \sum_{rs} \sum_{\mathbf{q}} \langle r | w^{h}(\mathbf{q}) | s \rangle d^{\dagger}_{r} d_{s} (b^{\dagger}_{\mathbf{q}} + b_{-\mathbf{q}}) \tag{4.14}$$

with

$$w^{\mathrm{e,h}}(\mathbf{q}) = \sqrt{\frac{\hbar q}{2V\rho v}} D^{\mathrm{e,h}} e^{-i\mathbf{q}\cdot\mathbf{r}_{\mathrm{e,h}}} \tag{4.15}$$

where ρ is the density of the material, $\hbar$ is the reduced Planck constant ($h/2\pi$), $D^{\mathrm{e,h}}$ are the deformation potentials for the electrons and the holes, v is the longitudinal sound velocity ($\hbar\omega_q = \hbar vq$) in the material, and $b_{\mathbf{q}}$ is the annihilation operator for an acoustic phonon with the momentum $\mathbf{q}$. The transition matrix element between the initial, Ψ_{I}, and final, Ψ_{F}, states can then be written as

$$\begin{aligned}\langle\Psi_{\mathrm{F}}|\,\hat{H}_{\mathrm{LA}}\,|\Psi_{\mathrm{I}}\rangle = &\sum_{ij}\langle\mathscr{L},N|c_i^\dagger c_j|N,\mathscr{R}\rangle w_{ij}^{\mathrm{e}}(\mathbf{q})\\ &+\sum_{rs}\langle\mathscr{L},N|d_r^\dagger d_s|N,\mathscr{R}\rangle w_{rs}^{\mathrm{h}}(\mathbf{q}).\end{aligned}\tag{4.16}$$

The initial phonon state is assumed to be the vacuum state with no phonons and the final phonon state is the state with one phonon with momentum $\mathbf{q}$. The other momentum states are empty. Hence, the process describes the electronic transition connected with a spontaneous emission of one phonon.

Fermi's golden rule can now be expressed using transition-density matrices as

$$\begin{aligned}\Gamma_{N,\mathscr{L}\leftarrow N,\mathscr{R}} = &\frac{2\pi}{\hbar}\int \mathrm{d}\mathbf{q}\left|\sum_{ij}\rho_{ij}^{\mathrm{e},\mathscr{L}\mathscr{R}}w_{ij}^{\mathrm{e}}(\mathbf{q})+\sum_{rs}\rho_{rs}^{\mathrm{h},\mathscr{L}\mathscr{R}}w_{rs}^{\mathrm{h}}(\mathbf{q})\right|^2\\ &\delta(E_{N,\mathscr{R}}-E_{N,\mathscr{L}}-\hbar\omega_q)\end{aligned}\tag{4.17}$$

where and $\delta(E_{N,\mathscr{R}} - E_{N,\mathscr{L}} - \hbar\omega_q)$ ensures that the energy condition is fulfilled. Summation over the orbital indices i, j and r, s, leads to a function of $\mathbf{q}$, the integral of which is most conveniently calculated in spherical coordinates.[53] The integral can then be evaluated analytically for the one angular variable, and numerically for the other angle. The radial coordinate is fixed due to conservation of the energy.[53] The methods to calculate the generalised transition-density matrices and phonon relaxations are related to those used in atomic and molecular electronic structure studies of one-photon transitions. The transition-density matrix preserving the many-body information of the phonon transition between $\mathscr{L}$ and $\mathscr{R}$ are obtained from the CI coefficients as[53,57]

$$\rho_{ij}^{\mathrm{e},\mathscr{L}\mathscr{R}} = \langle\mathscr{L},N|c_i^\dagger c_j|N,\mathscr{R}\rangle = \sum_I C_{I_j^i}^{N,\mathscr{L}}C_I^{N,\mathscr{R}}\tag{4.18}$$

$$\rho_{rs}^{\mathrm{h},\mathbf{LR}} = \langle\mathscr{L},N|d_r^\dagger d_s|N,\mathscr{R}\rangle = \sum_I C_{I_s^r}^{N,\mathscr{L}}C_I^{N,\mathscr{R}}\tag{4.19}$$

where the index I includes configurations in which orbital $j(s)$ is occupied and $I_j^i(I_s^r)$ refers to the configurations obtained from I by replacing the spin orbital $j(s)$ with $i(r)$. At coupled-cluster levels, the transition-density matrix can be obtained using response theory.[88–90]

C Radiative electron–hole recombination

The photon-emission rate $\Gamma_{N-1,\mathscr{L}\leftarrow N,\mathscr{R}}$, for the transition from a multiexciton complex with N electron-hole pairs $|N,\mathscr{R}\rangle$ to a complex with $(N-1)$ electron-hole pairs $|N-1,\mathscr{L}\rangle$ can be written as[53,82,91–93]

$$\Gamma_{N-1,\mathscr{L}\leftarrow N,\mathscr{R}} = \frac{ne^2E_pE_{ph}}{6\pi\hbar^2c^3\varepsilon_0m_{\mathrm{e}}}\sum_\sigma|\langle\mathscr{L},N-1|P_\sigma^-|N,\mathscr{R}\rangle|^2,\tag{4.20}$$

where n is the refractive index of the semiconductor, E_p is the Kane matrix element,[94] and E_{ph} is the emitted photon energy. The operator $P_\sigma{}^-$ is the inter-band polarisation operator[8] which annihilates an electron-hole pair with a given spin projection ($\sigma = \uparrow$ or $\downarrow$) by creating a photon with a definite circular polarisation. Configuration interaction expansions of the initial $\mathscr{R}$ and final $\mathscr{L}$ states yield a recombination density matrix expression for the photo-emission rate.

$$\Gamma_{N-1,\mathscr{L}\leftarrow N,\mathscr{R}} = \frac{ne^2E_pE_{ph}}{6\pi\hbar^2c^3\varepsilon_0m_{\mathrm{e}}}\sum_\sigma\left|\sum_{ir}\gamma_{ir,\mathscr{L}\mathscr{R}}^{\sigma,-\sigma}\langle i|r\rangle\right|^2,\tag{4.21}$$

where $\langle i|r\rangle$ is the overlap of the electron and hole orbitals. $\gamma_{ir,\mathscr{L}\mathscr{R}}^{\sigma,-\sigma}$, is the recombination density matrix given by

$$\gamma_{ir,\mathscr{L}\mathscr{R}}^{\sigma,-\sigma} = \langle\mathscr{L},N-1|c_id_r|N,\mathscr{R}\rangle = \sum_I C_I^{N-1,\mathscr{L}}C_{I_{ir}}^{N,\mathscr{R}},\tag{4.22}$$

the elements of which contain the many-body information about transitions between states with different numbers of charge carriers. The summation includes all configurations of the $\langle\mathscr{L},N-1|$ state ($C_I^{N-1,\mathscr{L}}$) and $C_{I_{ir}}^{N,\mathscr{R}}$ denotes the CI coefficients of the $|N,\mathscr{R}\rangle$ state that give a non-vanishing contribution when the electron in spin orbital i and the hole in spin orbital r are annihilated. The recombination density matrix can be evaluated for non-orthogonal states using the same ideas as used in atomic and molecular calculations of transition-density matrices.[95,96] The calculation of the recombination density matrix, $\gamma_{ir,\mathscr{L}\mathscr{R}}^{\sigma,-\sigma}$, requires only a small fraction of the computational time needed to obtain the CI coefficients of the $|N-1,\mathscr{L}\rangle$ and $|N,\mathscr{R}\rangle$ states.[55,97]

V. Calculations on self-assembled quantum dots

The strain-induced quantum-dot sample shown in Fig. 1 is formed in the InGaAs quantum well by the self-organising growth of an InP island on the InGaAs/GaAs semiconductor surface.[7] The diameter of the roughly cylindrical quantum dot is 80 nm and the width of the $\mathrm{In_{0.1}Ga_{0.9}As}$ quantum well is 7 nm. The confinement potential of the quantum dot can be calculated using the material parameters and the geometry of the sample.[6] The properties of the electrons and holes trapped in the confinement potential are obtained by solving the two-

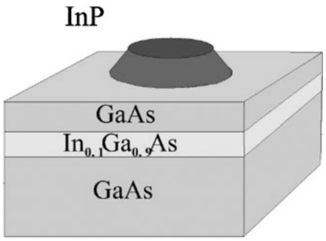

Fig. 1 The InP stressor on the surface of InGaAs/GaAs quantum-well sample leads to a confinement potential of electrons and holes in the $\mathrm{In_{0.1}Ga_{0.9}As}$ quantum well.

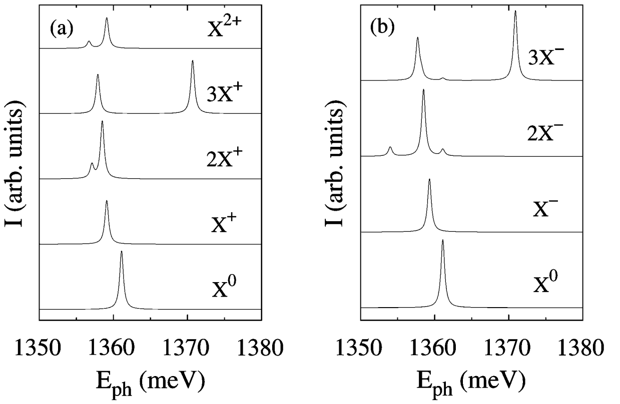

Fig. 2 The PL spectra calculated for (a) positively and (b) negatively charged multiexciton complexes confined in the InGaAs/GaAs quantum-dot. The spectrum of the neutral exciton is shown for comparison. In the notation nX^q, n is the number of electron-hole pairs and q is the excess charge.

band Schrödinger equation. The radiative recombination probabilities and luminescence energies were calculated at the full CI level for the neutral and charged exciton complexes as described in the previous section. The obtained luminescence spectra of charged multiexciton complexes in InGaAs/GaAs quantum dots are compared to the PL spectrum of the neutral exciton in Fig. 2. The spectra were simulated using the calculated luminescence energies and the corresponding radiative recombination transition probabilities calculated at the full CI level. Phonon couplings were not considered in the simulation of the spectra. For the positive quantum-dot samples, the energy of the strongest transition decreases when increasing the charge of the dot. For the doubly charged exciton system consisting of three holes and one electron, a weaker transition appears slightly below the main peak. For the negatively charged quantum-dot samples, the strongest transition is also redshifted as compared to the neutral one. The negative biexciton has two weak transitions, one lies on each side of the main luminescence peak. The luminescence spectra of the positive and negative triexcitons have two strong bands corresponding to σ–σ and π–π annihilations because the lowest σ shells are filled and the third electron-hole pair occupies the lowest π levels. In the spectrum of the negative triexciton, a weak transition slightly above the σ–σ peak is also seen in the spectrum. The calculated PL spectra resemble the experimental multiexciton emission spectra for an $In_{0.4}Ga_{0.6}As/GaAs$ quantum dot.[11] At high laser intensities, a large number of emission lines appear in the experimental spectra in the vicinity of the two strongest transitions, corresponding to the σ–σ and π–π bands.

The correlation effects are more important for quantum rings than for quantum dots because the repulsive part of the confinement potential at the centre of the quantum ring increases the energy of the σ states whereas the $\pi,\delta,\ldots$ states are less affected. The energy spacing between the one-particle states becomes smaller enabling a strong mixing of the states for the many-body systems. The correlation effects were studied for biexciton complexes confined in InGaAs/GaAs quantum-ring samples. The ring-shaped confinement potentials were constructed by adding a repulsive Gaussian function at the centre of the InGaAs/GaAs quantum dot. The strength of the repulsive potential at the ring centre is varied by adjusting a strength parameter; $\lambda = 0$ corresponds to the original quantum dot and $\lambda = 1$ yields a characteristic quantum ring. The radial confinement potentials of the electrons and holes for the λ values of 0.0, 0.4 and 0.8 are shown in Fig. 3.

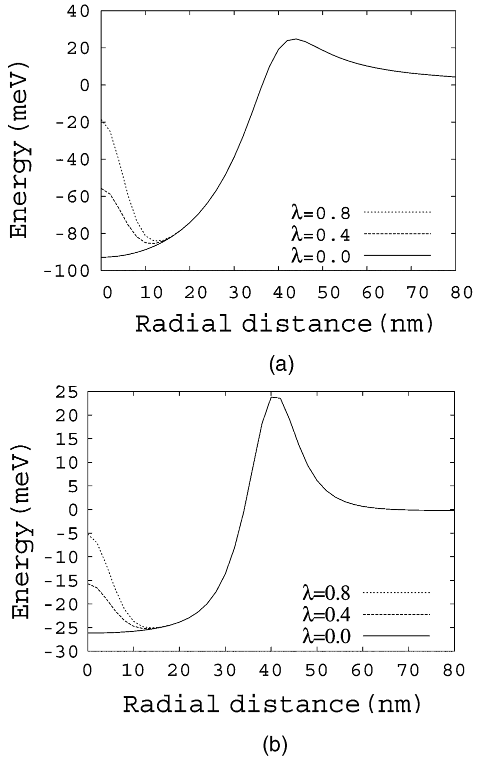

Fig. 3 The radial part of the confinement potentials of (a) the electrons and (b) the holes of the quantum dot ($\lambda = 0$) and the quantum rings ($\lambda = 0.4$ and $\lambda = 0.8$) are shown.

The total energy of the ground state of the biexciton complex confined in the GaAs semiconductor heterostructure was calculated as a function of the scaling factor λ. The energy increases by about 10% when increasing the repulsion potentials at the centre by letting λ go from $\lambda = 0$ to $\lambda = 1$. The correlation effects are found to be much larger in the quantum rings than in the dot. The difference in the correlation effect between the quantum dot and the quantum rings are illustrated in Fig. 4 where the occupation numbers of the Hartree–Fock reference are given as a function of potential strength parameter λ. The weight of the Hartree–Fock reference for the quantum dot is close to unity, whereas the Hartree–Fock reference contributes only 53% to the total wave function of the quantum ring obtained with $\lambda = 1.0$.

In the full CI calculations of the lowest excited states of the quantum-dot and quantum-ring samples, the splitting between the first excited state and the ground state decreases with increasing λ value. For the ring-shaped GaAs semiconductor heterostructure with $\lambda = 0.8$, the gap is less than 2 meV. In Fig. 5, we compare the excitation energies of the first few singlet excited states of the biexciton complexes confined in the

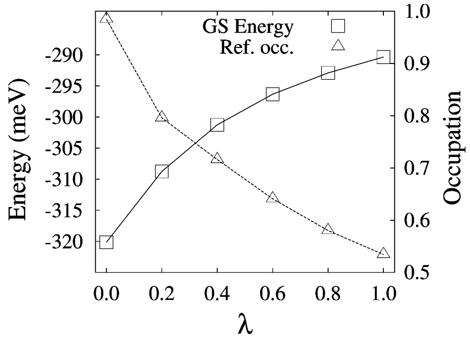

Fig. 4 The total energy of the biexciton complex as a function of the scaling parameter λ for the repulsive potentials at the dot centre. The occupation of the Hartree–Fock reference for quantum-dot and quantum-ring samples obtained for different λ values are also given.

quantum dot and the quantum rings with $\lambda = 0.4$ and $\lambda = 0.8$. In the figure, one can see that the excitation energies of the Π and Δ states decrease faster than for the excited Σ states when introducing the repulsive potentials at the dot centre. The small splittings between the ground state and the excited states of the quantum-ring samples indicate that the wave function can be drastically influenced by external perturbations.

VI. Molecular electronic structure methods

The two computational methods employed in the studies of the freestanding silicon nanoclusters are density functional theory (DFT) and low-order coupled-cluster (CC) theory. The calculations were performed with TURBOMOLE.[98] DFT was originally developed for computations of ground-state properties.[99,100] It was later extended to treat also time-dependent phenomena[101] using the time-dependent DFT (TDDFT) approach. Linear response TDDFT calculations provide excitation energies and transition strengths for electronic excitations. The adiabatic approximation and the use of the same functionals as employed in ground-state DFT calculations lead to some general shortcomings of the TDDFT approach.[19,102,103] TDDFT calculations have been found to underestimate the optical gap for short oligosilanes in the basis set limit. Hybrid functionals were found to partly correct this error. DFT calculations using hybrid functionals yield with moderate basis-set sizes excitation energies in good agreement with experimental values due to error compensation whereas in the basis-set limit the obtained optical gaps are about 0.3–0.4 eV too small as compared to experiment.[104] DFT calculations using functionals with Hartree–Fock exchange terms in the Hamiltonian are computationally more expensive. In the absence of explicit Hartree–Fock exchange, the electrostatic interaction can be approximated by using the resolution of the identity (RI), *i.e.* by expanding it in an auxiliary basis using the Coulomb norm.[105–108] The error introduced by the RI approximation is negligible but savings in computer time are 10–100 fold as compared to calculations using hybrid functionals.

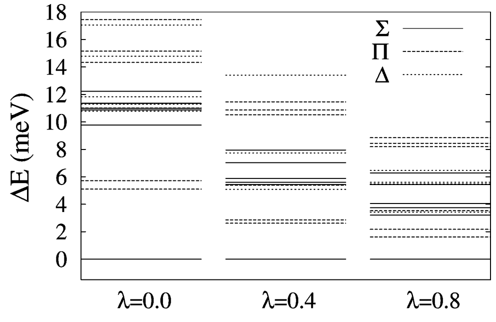

Fig. 5 The lowest calculated excitation energies of a biexciton complex confined in the quantum dot ($\lambda = 0$) and in two quantum-ring samples ($\lambda = 0.4$ and $\lambda = 0.8$) are shown. The ground-state energies of the biexciton complexes are set to zero.

The accuracy of CC calculations can in principle be systematically improved by employing higher-order CC models in combination with large basis sets. Unfortunately, the high computational costs render higher-order CC calculations on nanoclusters unattainable; only the lowest-order CC methods can be used. The CC singles model (CCS) provides the same excitation energies as obtained in CI singles (CIS) calculations, significantly overestimating the excitation energies. At the coupled-cluster approximate singles and doubles (CC2) level, the electron correlation is considered by an implicit treatment of the double excitations.[89,97] In the CC studies on the silicon nanoclusters, the CC2 model in combination with the RI approximation was used.[23,109,110] The excitation energies and transition moments of electronic transitions can be extracted from CC equations using the response approach[88] alternatively using the Lagrangian formulation which gives a variational expression for the CC energy with respect to the amplitude parameters.[89,90] The CC2 model with large enough basis sets has proven to be very accurate providing excitation energies of small oligosilanes in good agreement with experiment.[104]

VII. Calculations on freestanding silicon quantum dots

A Accuracy of TDDFT and CC2 calculations

In *ab initio* and DFT calculations of excitation energies, the two largest sources of uncertainties are the level of correlation treatment and the size of the one-particle basis sets. The reliability of the employed computational level and the accuracy of the employed functional can be assessed by increasing the size of the one-particle basis set until it is practically complete and then compare the obtained excitation energies with available experimental data. Such a benchmarking procedure for linear silanes showed that the optical gaps calculated at the CC2 level agree well with experimental values for Si_2H_6 and Si_3H_8 measured in the gas phase, whereas for SiH_4 the discrepancy between calculated and measured values is as much as 0.7 eV.[104] See Fig. 6. However, CC3 calculations showed that the reported experimental excitation threshold of 8.8 eV for SiH_4 does not correspond to a vertical excitation.[111] The best estimated value based on CC3 results for the vertical excitation energy is 9.45 eV.[104] The small difference of 0.18 eV between the CC2 and CC3 excitation energies for SiH_4 and the almost perfect agreement with experimental data for Si_2H_6 and Si_3H_8 show that the CC2 model works rather well for silanes and most likely also for silicon nanoclusters. For Si_4H_{10}, Si_5H_{12}, and neo-Si_5H_{12}, the first excitation energies

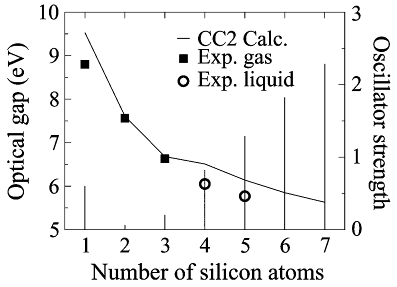

Fig. 6 The optical gap (in eV) of linear silanes calculated at the CC2 level with Dunning's quadruple ζ basis set augmented with diffuse and polarisation functions (aug-cc-pV(Q + d)Z)[113] are compared to experimental values. The calculated oscillator strengths are given as histograms.

calculated at the CC2 level are 0.46, 0.37 and 0.34 eV larger than the experimental values measured in the liquid phase.[112] The large differences are most likely due to solvent effects.

In DFT studies on the linear silanes using LDA and GGA density functionals, the optical gaps are underestimated by 0.7–0.8 eV as compared to the CC2 values.[104] Hybrid functionals such as the Perdew–Burke–Ernzerhof hybrid functional (PBE0)[114] and Becke's three parameter functional with the Lee–Yang–Parr correlation functional (B3LYP)[115,116] perform better. For silanes and silicon nanoclusters, the hybrid functionals seem to be a good compromise as far accuracy and computational costs are concerned. At the PBE0 level, the optical gaps of the linear silanes are about 0.3 eV smaller than the corresponding CC2 values. The optical gaps calculated at different levels are compared in Fig. 7. Since the excitation energies obtained at the DFT levels are systematically too small as compared to experiment, better estimates for the optical gaps can be deduced from the DFT excitation threshold by adding a constant shift.

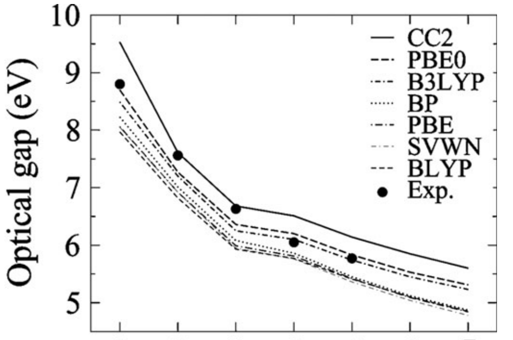

Fig. 7 The optical gap (in eV) of linear silanes calculated at the CC2 and DFT levels using the aug-cc-pV(Q + d)Z basis sets.

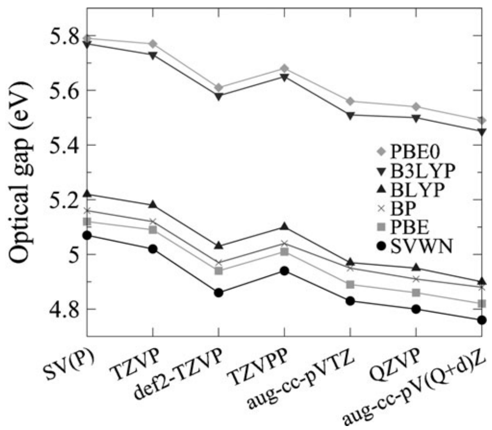

Fig. 8 The optical gap (in eV) of $Si_{10}H_{16}$ calculated at DFT levels using different basis sets. SV(P) = split valence basis set with one set of polarisation functions on Si.[118] TZVP = triple ζ valence basis set with one set of polarisation functions.[119] def2-TZVP = the newly optimised TZVP.[120] TZVPP = triple ζ valence basis set with two sets of polarisation functions.[119] Aug-cc-pVTZ = correlation consistent basis set of valence triple ζ quality augmented with diffuse functions.[121] QZVP = quadruple ζ valence with one set of polarisation functions.[122] Aug-cc-pV(Q + d)Z = correlation consistent basis set of valence quadruple ζ quality augmented with diffuse functions and with an extra *d* shell on Si.[113]

In the silicon nanocluster studies, the aug-cc-pV(Q + d)Z basis sets cannot be employed because the computational costs become huge. The use of smaller basis sets usually blueshift the lowest electronic transitions. PBE0 calculations with triple ζ quality basis sets augmented with polarisation functions (TZVP) were found to yield optical gaps for the silanes in close agreement with experiment due to cancellation of errors.[48,104] The basis-set convergence of the optical gap of the $Si_{10}H_{16}$ cage is shown in Fig. 8 and 9. The optical spectrum for the recently synthesised sila-adamantane cluster capped with methyl and trimethylsilyl groups ($Si_{14}C_{24}H_{72}$) has a strong absorption maximum at 5.59 eV.[117] DFT calculations at the PBE0/TZVP level yielded an optical gap of 5.06 eV. As the first few transitions are rather weak, the observed transition probably corresponds to the two strong bands at 5.54 and 5.60 eV with oscillator strengths of 0.42 and 0.69, respectively.[48]

The molecular structure of the silicon nanocluster also affects the calculated optical gap. The first excitation energy of SiH_4 calculated using the experimental structure is 0.1 eV larger than obtained with the structure optimised using the Becke–Perdew (BP) functional and TZVP basis sets[123–125]

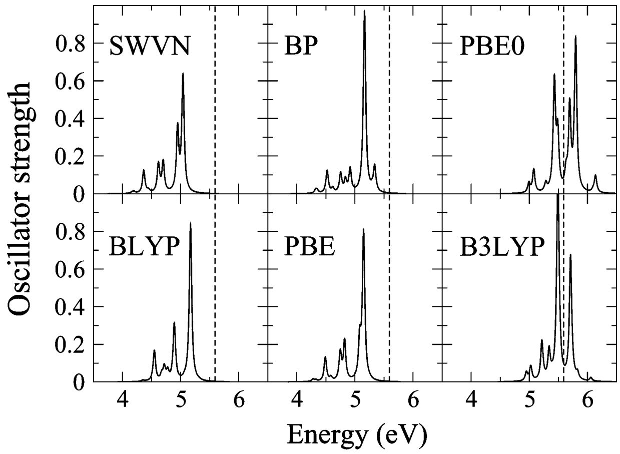

Fig. 9 Simulated absorption spectra of $Si_{14}C_{24}H_{72}$ obtained with different functionals and def2-QZVP basis sets. The experimental absorption peak maximum is indicated with the vertical dashed line.

implying that a better precision than 0.1 eV cannot be expected for the calculated excitation energies.

Many other computational methods have been used to predict the optical gap of silicon nanoclusters. These studies comprise highly accurate calculations at the many-body GW-BSE (Wigner's method for solving the Bethe–Salpeter equations using Green's function theory)[126–128] and quantum Monte Carlo (QMC) levels.[16,127,129,130] The QMC is in principle a very accurate many-body approach that can be applied to silicon nanoclusters consisting of hundreds of atoms.[131,132] However, the QMC approach is not quite unproblematic for excited state studies because the construction of the trial function is not trivial and the obtained results might significantly depend on that choice.[130] For SiH_4, the best optical gap obtained with the QMC is 9.47(2) eV[129] which is in excellent agreement with the best *ab initio* value of 9.45 eV calculated at the CC3 level.[104] For SiH_4, a smaller optical gap of 9.1(1) eV has also been obtained at the QMC level.[127] For larger clusters, the choice of the trial function is unfortunately not easier than for a small molecule. As a consequence, optical gaps calculated for silanes at the QMC level are not always mutually concordant.[16,128–130] However, the QMC optical gaps for the neo-Si_5H_{12} molecule possessing T_d symmetry and for the sila-adamantane ($Si_{10}H_{16}$) cluster calculated by Benedict *et al.*[128] agree well with the best *ab initio* excitation energies and with estimated experimental gas-phase values.[48,104] The assignment of the electronic excitation spectra using QMC calculations is difficult because the band strengths are not readily obtained at that level.

The optical gap calculated at the TDDFT level using LDA and GGA functionals becomes equal to the HOMO–LUMO splitting in the limit of infinitely large clusters. For clusters larger than 0.8 nm, the difference between the excitation threshold and the HOMO–LUMO gap is at the BP TDDFT level less than 0.1 eV and for silicon nanoclusters larger than 1.7 nm in diameter, the difference is less than 0.01 eV.

Fig. 10 shows a combination of optical gaps calculated at the BP TDDFT level and the luminescence energies obtained at the effective mass approximation (EMA) level. The EMA data are taken from ref. 25. The gaps calculated at the BP TDDFT level using TZVP basis sets are shifted by 0.8 eV. This shift is chosen such that the first excitation energy for $Si_{10}H_{16}$ obtained at the BP TDDFT level agrees with the accurate optical gap of 5.95 eV estimated using CC2 and QMC calculations. The dashed line in Fig. 10 represents the optical gaps calculated at the QMC level using the diffusion Monte-Carlo (DMC) approach.[16]

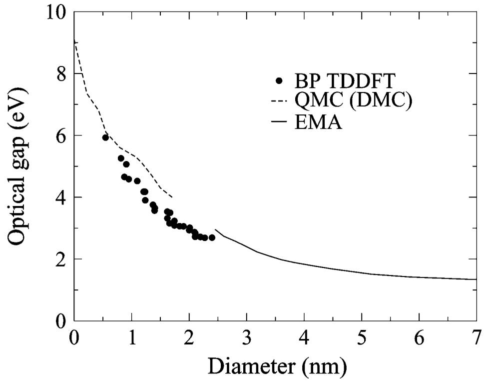

Fig. 10 The optical gap (in eV) of silicon nanoclusters as obtained at the BP TDDFT and EMA levels. The BP TDDFT optical gaps are shifted by 0.8 eV to yield the correct optical gap for $Si_{10}H_{16}$. The QMC and EMA optical gaps are taken from ref. 16 and 25.

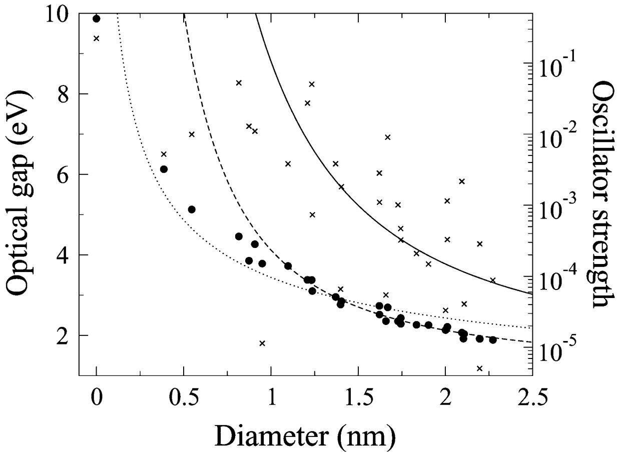

Fig. 11 Optical gaps (●, in eV) and oscillator strengths (×) for silicon clusters of different size as a function of the cluster diameter calculated at the BP TDDFT level using the def2-SV(P) basis set. The size dependence of the optical gap fitted using the BP TDDFT data is shown as a dashed line. The experimental fit is represented with the dotted line. The solid line shows size dependence of the calculated oscillator strength obtained using the fitting procedure described in the text.

The optical gaps calculated at the BP TDDFT level using def2-TZVP basis sets for hydrogen-capped silicon nanoclusters are summarised in Fig. 11. In the DFT and TDDFT calculations, the TURBOMOLE split valence basis set augmented with polarisation functions were employed.[120] The analytical expression for the size dependence of the optical gap of silicon nanoclusters was obtained from the BP TDDFT optical gaps (E_g) of hydrogen-capped nanoclusters larger than 1 nm by using a power-law fit. The fitted expression for the size dependence of the optical gap is

$$E_g = 1.12 + 3.00(d[\text{nm}])^{-1.575}, \qquad (7.23)$$

where d is the cluster diameter in nanometers and 1.12 eV is the assumed bandgap for bulk silicon. Belomoin *et al.*[64] reported a size dependence of $E_g = 3.44(d[\text{nm}])^{-0.5}$ which was obtained by fitting to experimental PL energies of four nanoclusters. Delerue *et al.* proposed a size-dependence of $E_g = 1.12 + 3.73(d[\text{nm}])^{-1.39}$ based on PL results and calculations.[133] Meier *et al.*[134] determined the size-dependence of the oscillator strength by measuring the PL decay rates of silicon nanoclusters of different size. The cluster sizes were estimated from the size-dependence of the optical gap using the fit of Delerue *et al.*

The oscillator strengths calculated at the BP TDDFT level for the first electronic transition are shown in Fig. 11. The calculated oscillator strengths decrease less systematically with increasing cluster diameter than the excitation energy. A clear trend is though seen in the graph. The curve describing the size dependence of the oscillator strengths was obtained by first

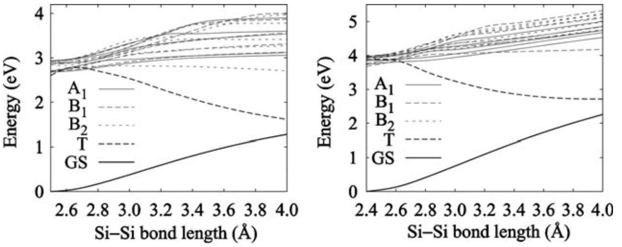

(a) (b)

Fig. 12 The potential energy curves for the surface dimer are shown for the singlet ground state (GS), the lowest triplet state (T), and the five lowest excited states of each irreducible representation attainable by dipole transitions from the ground-state. The potential energy surfaces are shown for (a) $Si_{29}H_{24}$ and (b) $Si_{29}H_{34}$ as a function of the dimer elongation. A_1, B_1, and B_2 denote the symmetry representations of the excited states.

determining the energy dependence of the oscillator strengths (f_{osc}) using a similar analytical expression as used by Meier *et al.*[134] The obtained expression is

$$f_{osc} = 0.1351 \times 10^{-6} \exp(E_g[eV]/0.3036). \qquad (7.24)$$

Combining eqn (7.24) with the fitted expression in eqn (7.23) yields the following expression for the size dependence of the oscillator strength

$$f_{osc} = 0.5406 \times 10^{-5} \exp(9.881/d[nm]^{1.575}). \qquad (7.25)$$

The curve representing eqn (7.25) is drawn as a solid line in Fig. 11. A similar expression with the coefficients of 1.4×10^{-6}, 11.24, and 1.39 was obtained by Meier *et al.*[134] using experimental PL life times in combination with the size dependence of the absorption energy calculated by Delerue *et al.*[133] The analytical expressions obtained using the two fitting procedures agree well. The oscillator strengths obtained for the larger hydrogen-capped silicon nanoclusters are indeed very small but they agree qualitatively with the experimental data of Meier *et al.*[134] The size-dependence function for the oscillator strength indicates that the large oscillator strengths of about unity obtained for the very bright silicon nanoclusters are most likely not merely due to confinement effects.

A surface dimer model suggested by Allan *et al.*[68] has often been used in explaining the luminescence of silicon nanoclusters (see *e.g.* ref. 135–137). We have performed calculations with two clusters $Si_{29}H_{34}$ and $Si_{29}H_{24}$ and investigated the potential energy surface as a function of the elongation of a single dimer on the surface while optimising other structural degrees of freedom but preserving C_{2v} symmetry. The results obtained at the BP TDDFT level using the def2-TZVP basis sets are shown in Fig. 12. Neither of the surface dimers exhibits a double-well potential, contrary to the results obtained by Allan *et al.* Additionally, the oscillator strengths at elongated geometries are of the order of magnitude of 0.01 at most. Therefore, the dimer model is, if not wrong, at least questionable. Interestingly, the potential energy surface of the triplet ground state for the surface dimer in $Si_{29}H_{24}$ does have a double well character.

B Hydrogen-capped silicon nanoclusters

Silicon nanoclusters covered by hydrogens can be synthesised through electrochemical etching with hydrofluoric acid.[4,64,66,138–140] Luminescent silicon nanoclusters can also be synthesised from NaSi.[26,141] By letting NaSi react with NH_4Br, Zhang *et al.* manufactured slightly larger hydrogen-capped silicon nanoclusters with an average diameter of 3.9 ± 1.3 nm exhibiting strong PL at 438 nm.[141] An alternative route to synthesise hydrogen-capped silicon nanoclusters is by reducing Si^{4+} ions in micelles by $LiAlH_4$.[30] The growth of the clusters is restricted by the micelle size. The smallest clusters are 1.8 nm in diameter and consist of *ca.* 150 Si atoms covered by hydrogens.

Even though the hydrogen-capped silicon nanoclusters have been studied computationally at many levels of theory,[15–17,45,48,64,73,128–130,136,140,142–160] the reason for their strong PL emission is still unresolved. A consensus concerning the molecular structure of the manufactured 1 nm nanoclusters has not been reached either. The most popular candidates for the structure of the 1 nm silicon nanocluster are $Si_{29}H_{24}$, $Si_{29}H_{36}$, and $Si_{35}H_{36}$ shown in Fig. 13. However, their absorption and emission energies as well as the band strengths do not agree well with experimental observations. The absorption thresholds for $Si_{29}H_{24}$, $Si_{29}H_{36}$, and $Si_{35}H_{36}$ calculated at the DFT level using the BP functional are 2.74, 3.84 and 3.70 eV, respectively.[17] The B3LYP DFT, BP DFT and CC2 calculations yield an estimated optical gap of about 4.5 eV for $Si_{29}H_{36}$ which is significantly larger than the experimental excitation threshold of 3.7 eV.[144] The corresponding QMC value is 5.3 eV.[16] A similar extrapolation procedure for $Si_{29}H_{24}$ and $Si_{35}H_{36}$ as done for $Si_{10}H_{16}$ in section VIIA yields excitation thresholds of 3.6 and 4.3 eV as compared to the QMC optical gaps of 3.6 and 5.1 eV, respectively.[16,128]

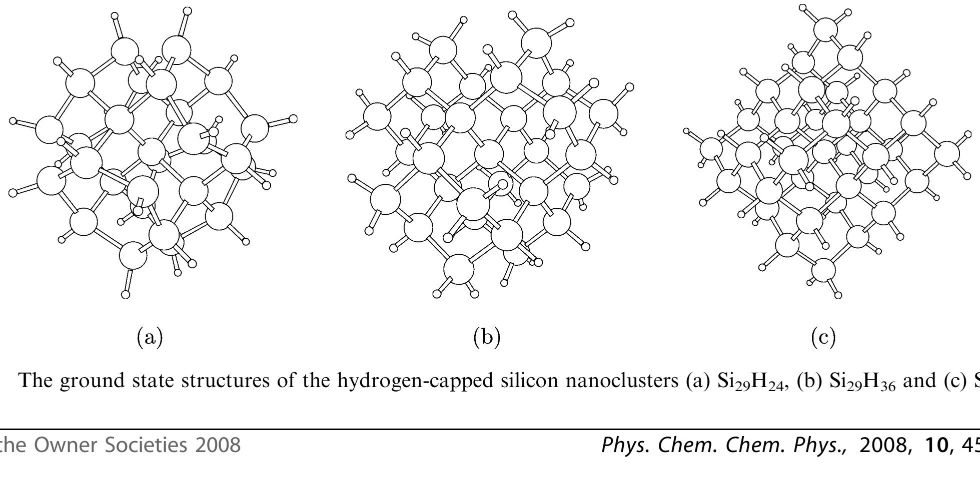

(a) (b) (c)

Fig. 13 The ground state structures of the hydrogen-capped silicon nanoclusters (a) $Si_{29}H_{24}$, (b) $Si_{29}H_{36}$ and (c) $Si_{35}H_{36}$.

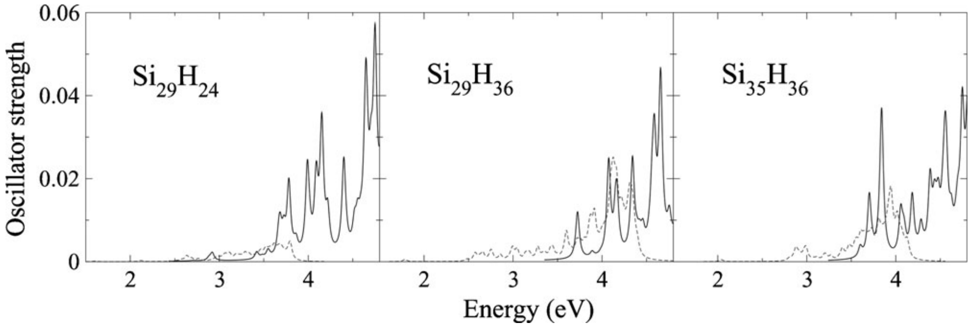

Fig. 14 The electronic excitation spectra of $Si_{29}H_{24}$, $Si_{29}H_{36}$ and $Si_{35}H_{36}$ calculated at the BP TDDFT level using the def2-TZVP basis set. The solid line shows the absorption spectra obtained using the optimised ground-state structure and the dashed line is obtained using the optimised geometry of the first excited state. The spectra using the excited state structure were not calculated for the whole energy range shown.

The electronic excitation spectra for $Si_{29}H_{24}$, $Si_{29}H_{36}$ and $Si_{35}H_{36}$ in Fig. 14 were obtained by plotting each excitation energy using a Lorentzian line shape function as given in eqn (3.1). In the absorption spectra one sees that the first transitions are very weak and that at higher energies, states with stronger absorption intensity appear. However, no very bright states were obtained in the calculations. The oscillator strengths of 10^{-3}–10^{-2} for these transitions are two to three orders of magnitude smaller than those observed experimentally.[74]

The PL energy and Stokes shifts can be obtained in TDDFT calculations using the cluster structure of the excited state. The corresponding oscillator strengths provide an estimate for the PL strength. For $Si_{29}H_{36}$, the optimisation of the excited state structure in D_{2d} symmetry yielded a Stokes shift of 0.7 eV,[17,73] whereas a more recent calculation without any symmetry constraints resulted in a totally unsymmetric structure (C_1) and a large Stokes shift of 2 eV. For the two other clusters, the Stokes shifts are 1.1 and 1.6 eV, respectively. The vertical excitation and de-excitation energies for $Si_{29}H_{24}$, $Si_{29}H_{36}$ and $Si_{35}H_{36}$ are summarised in Table 2. The Stokes shifts and the two relaxation contributions are also given. The oscillators strengths obtained for the excited state structures are significantly smaller than obtained for the ground-state structures, especially for the two larger clusters.

Computational studies on sila-adamantane based silicon nanoclusters showed that the oscillator strengths are practically independent of the interior structure of the cluster.[48] Clusters with fused sila-adamantane cages as core have very weak transitions[48] even though sila-adamantane was found to have strong absorption at 5.6 eV.[48,117] Reboredo *et al.*[156] also reported that the surface chemistry of silicon nanoclusters is independent of the core structure. Thus, most likely none of the studied silicon nanoclusters is responsible for the observed strong blue PL corresponding to an oscillator strength of 0.92.[74]

Table 2 The excitation energies (in eV) for the Si nanoclusters calculated at the BP/def2-TZVP level using the ground-state (E_{gs}) and the first excited state (E_{es}) structures. The Stokes shift (ΔE_{stokes}) and its contributions from the strain of the ground-state (ΔE_{gs}) and the relaxation of the excited state (ΔE_{es}) are also given. f_{gs} and f_{es} denote the oscillator strengths of the corresponding transitions

	$Si_{29}H_{24}$	$Si_{29}H_{36}$	$Si_{35}H_{36}$
E_{gs}	2.70	3.72	3.60
E_{es}	1.61	1.79	2.04
ΔE_{stokes}	1.10	1.94	1.56
ΔE_{gs}	0.70	1.33	1.20
ΔE_{es}	0.40	0.61	0.36
f_{gs}	0.000089	0.011	0.0025
f_{es}	0.00015	0.00052	0.00045

Optimisations of the cluster structures for the first excited state show that many local minima with completely different Stokes shifts can occur on the PES of the excited states. The large experimentally observed Stokes shift has been explained by localised surface states in the silicon nanocluster.[68] Allan *et al.* proposed that such states exist under the form of self-trapped excitons at the Si–Si dimers on the nanocluster surface. However, in the optimisations of the cluster structures for the excited state, we did not obtain any significantly elongated Si–Si bonds. Thus, our silicon nanocluster studies do not support the notion that surface dimers are the light emitters of hydrogen-capped silicon clusters.

Fig. 15 illustrates changes in the Si–Si bond lengths of the $Si_{29}H_{36}$ structure upon excitation. The largest structural changes (0.095–0.050 Å) occur at the cluster surface while changes inside the cluster core are slightly smaller (0.045–0.039 Å). The largest decrease in the bond lengths of −0.012 Å occurs also at the cluster surface.

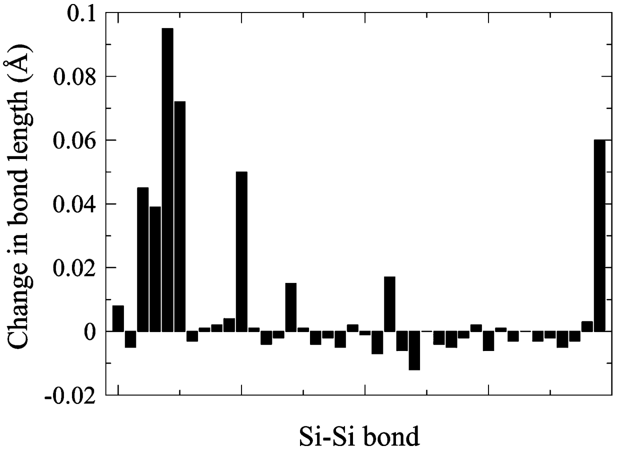

Fig. 15 Changes in Si–Si bond lengths due to structural relaxations of the ground-state structure upon excitation to the lowest excited state of the $Si_{29}H_{36}$ cluster calculated at BP DFT and BP TDDFT levels using the def2-TZVP basis set.

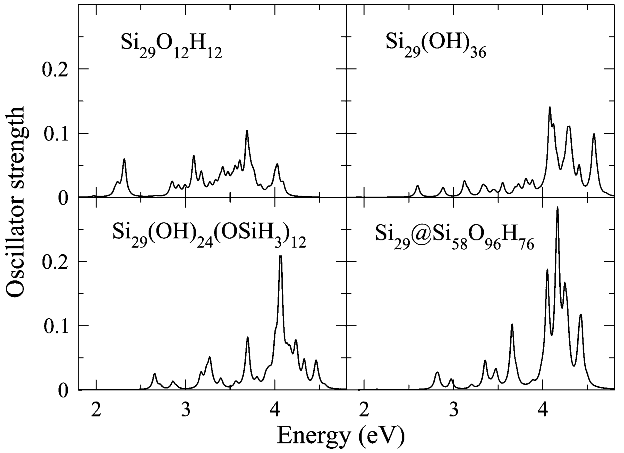

Fig. 16 The electronic excitation spectra of the oxidised silicon nanoclusters calculated at BP DFT level using the TZVP basis set.

C Oxidised silicon nanoclusters

Silicon nanoclusters prepared through electrochemical dispersion are mainly capped by hydrogens after the etching.[4,66,161] They also contain a small amount of impurity atoms[66,145] and the surface is partly oxidised.[4] The synthesised silicon nanoclusters react in the presence of molecular oxygen increasing the silicon oxide coverage of the cluster surface.[76] The oxidation leads to a significant redshift of the PL.[162,163] The quantum yield is also much lower for the oxidised clusters.[76] Measurements of the PL of oxidised silicon nanoclusters display emission contributions that can be assigned to Si–O–Si and Si=O groups.[161,163,164] The spontaneous oxidation also forms –OH groups on the surface.[76]

The calculated electronic absorption spectrum in Fig. 16 shows that the optical gap for the oxidised $Si_{29}(OH)_{36}$ cluster is redshifted by about 1.5 eV as compared to the hydrogen-capped one. The first band of the calculated absorption spectrum consists of several transitions and it has an oscillator strength maximum of 0.06. The oscillator strength for the oxidised cluster with Si=O groups on the surface is thus larger than obtained for the hydrogen-capped ones. The oscillator strength is still about 15 times smaller than obtained experimentally for the hydrogen-capped silicon nanocluster samples.[74] The optical gap calculated for $Si_{29}(OH)_{36}$, which is a silicon nanocluster capped by 36 hydroxyl (–OH) groups, is about 1 eV smaller than for the corresponding hydrogen-capped one. The band strengths for the hydroxyl-capped silicon nanocluster are of the same size as for the hydrogen-capped silicon nanocluster. Vasiliev *et al.*[162] obtained similar results in their computational study. The oscillator strengths for the lowest transitions of the absorption spectrum of $Si_{29}(OH)_{24}(OSiH_3)_{12}$ are also of the same size as obtained for the hydroxyl terminated cluster. A silicon cluster embedded in silica was also investigated. The silica is modelled by a $Si_{58}O_{96}H_{76}$ shell surrounding the Si_{29} core. Its electronic absorption spectrum shown in Fig. 16 is redshifted by about 1 eV as compared to hydrogen-terminated Si_{29}. The obtained oscillator strengths for the lowest transitions of $Si_{29}@Si_{58}O_{96}H_{76}$ are as weak, as obtained for the oxidised silicon nanoclusters.

D Silane-capped silicon nanoclusters

The computational studies on hydrogen-capped silicon nanoclusters show that their optical gaps are somewhat larger than obtained in the experiment. The calculated Stokes shifts are also larger than the experimental values. The calculations show that strong ground-state transitions are lacking among the low-lying excited states. The benchmark studies on the linear silanes[104] as well as the calculated and measured absorption spectra of silyl and methyl capped sila-adamantane[117] suggest that strongly emitting silicon nanoclusters can be designed by attaching molecular functional groups to the cluster surface where the substituents function as light emitters. Based on semiempirical calculations, Takeda *et al.* suggested that oligosilane bridged silicon nanoclusters might be the origin of the PL of porous silicon.[165] Luterova *et al.*,[166,167] and Schauer *et al.*[79] studied experimentally the PL of porous silicon samples and found that $-(SiH_2)_n-$ units might form efficient luminescence centres in these materials. Mu *et al.*[168] also reported strong blue PL from large silica nanospheres covered by chlorotrimethylsilane.

Recent DFT calculations on silicon nanoclusters covered by linear silane groups support this conception.[158] The calculations showed that these structures have significantly larger oscillator strengths for the lowest electronic transitions than obtained for the hydrogen-capped ones. The obtained optical gaps are rather independent of the length of the silane chain, whereas the oscillator strength increases linearly with its length.

The BP TDDFT calculations on the dimers consisting of two $Si_{29}H_{36}$ clusters bridged by a silane chain indicate that such structures might be responsible for the strong light emission observed for nano-sized silicon structures.[158] The dimers have low-lying strong transitions, the energy of which is almost independent of the length of the silane bridge. On the other hand, the oscillator strength is linearly proportional to the number of Si atoms in the chain. The size of the cluster tunes the absorption wavelength, whereas the silane bridge functions as an 'antenna'. The excitation energies and the corresponding oscillator strengths for $Si_{29}H_{35}-(SiH_2)_n-Si_{29}H_{35}$ are shown in Fig. 17.

The calculations on the silane-capped silicon nanoclusters show that variations in the cluster structure do not significantly affect the wavelength of the PL, whereas the emission strength are strongly dependent on the presence and character of the substituents. This could explain why only a few percent of the nanoclusters are found to be luminescent in experimental studies.[71,161,169] The PL properties of a silicon nanocluster could even be tailored by attaching appropriate substituents to the cluster surface.[1,161] Light emitting substituents could also explain the dissimilar results obtained for the relation between the size of the silicon nanocluster and the observed luminescence energies.[30,149]

VIII. Outlook

Research on semiconductor quantum dots has steadily increased over the past two decades and concrete applications have also began to emerge. Many questions are still

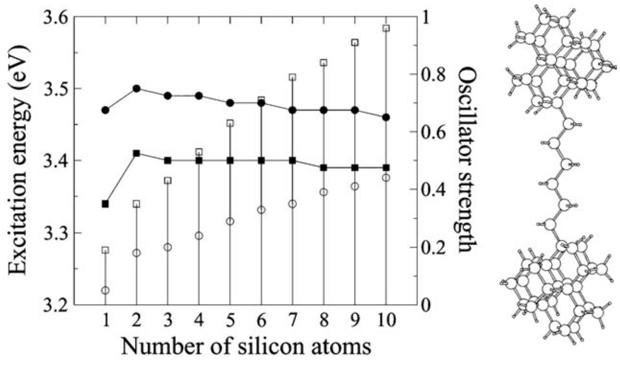

(a) (b)

Fig. 17 (a) The excitation energies (in eV) of the two lowest transitions and the corresponding oscillators strengths for the silane-bridged silicon-nanocluster dimers obtained at the BP TDDFT level shown as a function of the number of –SiH_2– units in the bridge. The filled symbols show the excitation energies and histograms the oscillator strengths. (b) A silane-bridged dimer with six –SiH_2– units in the bridge.

unanswered and more experimental and computational work is needed before the full potential of quantum dots can be utilized. Silicon has established its position as the most used semiconductor material due to several beneficial properties as compared to other materials, whereas semiconductor bulk materials with direct band gaps have to be used to achieve efficient optical devices. In comparison to bulk semiconductors, the charge carriers of the quantum dots are spatially confined in all dimensions, reducing the dimensionality of the quantum system and bringing out new kind of physical phenomena. As the surface to volume ratio for quantum dots is non-negligible, the surface properties of the free-standing quantum dots or the chemical bonds to the surrounding bulk material at the interface of the embedded quantum dots influence their light-emission quality. Even though bulk silicon with its indirect band gap has poor optical properties, small silicon nanoclusters have been found to be strongly fluorescent. The brightly luminescent silicon nanostructures are novel candidates for new light-emitting devices. Many theoretical and technological problems still remain to be tackled before silicon based optical devices are in everyday use. People have argued that silicon will never be a useful optical material, but the recent progress towards silicon-based light sources and devices is beginning to convince the most ardent critics.

The size of the quantum dots spans several length scales implying that different types of computational approaches are required to model them. The smallest quantum dots consisting of up to few tens of atoms can today be studied at *ab initio* correlated levels, whereas DFT based methods can be employed in calculations on quantum dots consisting of hundreds of atoms. Faster computers and more efficient algorithms will bring ever increasing size of quantum dots within reach of DFT calculations. Atomistic computations on large embedded quantum dots, quantum-dot molecules, quantum rings, and more general semiconductor nanostructures will in the nearest future be unfeasible. The optical properties of such systems can be provided by EMA calculations, which are explicitly considering the correlated motion of the confined electrons and holes of the multiexciton complex.

Acknowledgements

This research has been supported by the Academy of Finland through its Centers of Excellence Programme 2006–2011 and the OPNA research project (118195).

References

1. J. G. C. Veinot, *Chem. Commun.*, 2006, 4160–4168.
2. A. Zunger, *MRS Bull.*, 1998, **23**, 35–42.
3. Z. Yamani, S. Ashhab, A. Nayfeh, W. H. Thompson and M. Nayfeh, *J. Appl. Phys.*, 1998, **83**, 3929–3931.
4. G. Belomoin, J. Terrien and M. H. Nayfeh, *Appl. Phys. Lett.*, 2000, **77**, 779–781.
5. L. Dal Negro, J. H. Yi, J. Michel, L. C. Kimerling, S. Hamel, A. Williamson and G. Galli, *IEEE J. Sel. Top. Quantum Electron.*, 2006, **12**, 1628–1635.
6. J. Tulkki and A. Heinämäki, *Phys. Rev. B: Condens. Matter Mater. Phys.*, 1995, **52**, 8239–8243.
7. H. Lipsanen, M. Sopanen and J. Ahopelto, *Phys. Rev. B: Condens. Matter Mater. Phys.*, 1995, **51**, 13868–13871.
8. L. Jacak, P. Hawrylak and A. Wojs, *Quantum Dots*, Springer, Berlin, 1998.
9. F. Boxberg and J. Tulkki, *Rep. Prog. Phys.*, 2007, **70**, 1425–1471.
10. M. A. Reed, R. T. Bate, K. Bradshaw, W. M. Duncan, W. Frensley, J. W. Lee and H. D. Smith, *J. Vac. Sci. Technol., B*, 1998, **4**, 358–360.
11. A. Zrenner, *J. Chem. Phys.*, 2000, **112**, 7790–7798.
12. J. M. Luttinger and W. Kohn, *Phys. Rev.*, 1955, **97**, 869–883.
13. M. Braskén, M. Lindberg, D. Sundholm and J. Olsen, *Phys. Rev. B: Condens. Matter Mater. Phys.*, 2000, **61**, 7652–7655.
14. D. Rappoport and F. Furche, in *Time-Dependent Density Functional Theory*, ed. M. A. L. Marques, C. A. Ullrich, F Nogueira, A Rubio, K Burke and E. K. Gross, number 706 in *Lecture Notes in Physics*; Springer-Verlag, 2006, pp. 337–354.
15. A. Puzder, A. J. Williamson, J. C. Grossman and G. Galli, *J. Chem. Phys.*, 2002, **117**, 6721–6729.
16. A. Williamson, J. C. Grossman, R. Q. Hood, A. Puzder and G. Galli, *Phys. Rev. Lett.*, 2002, **89**, 196803.
17. O. Lehtonen and D. Sundholm, *Phys. Rev. B: Condens. Matter Mater. Phys.*, 2005, **72**, 085424.
18. C. Hättig, in *Computational Nanoscience: Do It Yourself!*, ed. J Grotendorst, S Blugel and D Marx, NIC series, Jülich, 2006, vol. 31, pp. 245–278.
19. F. Furche and K. Burke, in *Annual Reports in Computational Chemistry, 1*, ed. D Spellmeyer, Elsevier, Amsterdam, 2005, pp. 19–30.
20. F. Furche and D. Rappoport, in ch. III of *Computational Photochemistry*, vol. 16 of *Computational and Theoretical Chemistry*, ed. M Olivucci, Elsevier, Amsterdam, 2005.
21. F. Furche and R. Ahlrichs, *J. Chem. Phys.*, 2002, **117**, 7433–7447.
22. C. Hättig and A. Köhn, *J. Chem. Phys.*, 2002, **117**, 6939–6951.
23. C. Hättig and F. Weigend, *J. Chem. Phys.*, 2000, **113**, 5154–5161.
24. M. Cardona and F. H. Pollak, *Phys. Rev.*, 1966, **142**, 530–543.
25. G. Nesher, L. Kronik and J. R. Chelikowsky, *Phys. Rev. B: Condens. Matter Mater. Phys.*, 2005, **71**, 035344.
26. S. Lee, W. J. Cho, Y. D. Kim, E. K. Kim and J. G. Park, *Jpn. J. Appl.Phys., Part 2*, 2005, **44**, 5843–5846.
27. P. F. Trwoga, A. J. Kenyon and C. W. Pitt, *J. Appl. Phys.*, 1998, **83**, 3789–3794.
28. J. W. Luo, S. S. Li, J. B. Xia and L. W. Wang, *Appl. Phys. Lett.*, 2006, **88**, 143108.
29. G. Pellegrini, G. Mattei and P. Mazzoldi, *J. Appl. Phys.*, 2005, **97**, 073706.
30. J. P. Wilcoxon, G. A. Samara and P. N. Provencio, *Phys. Rev. B: Condens. Matter Mater. Phys.*, 1999, **60**, 2704–2714.
31. C. Delerue, G. Allan and M. Lannoo, *J. Lumin.*, 1998, **80**, 65–73.
32. L. E. Brus, *J. Chem. Phys.*, 1983, **79**, 5566–5571.

33. L. E. Brus, *J. Chem. Phys.*, 1984, **80**, 4403–4409.
34. Y. Kayanuma, *Phys. Rev. B: Condens. Matter Mater. Phys.*, 1988, **38**, 9797–9805.
35. Y. Kayanuma, *Phys. Rev. B: Condens. Matter Mater. Phys.*, 1991, **44**, 13085–13088.
36. A. L. Efros and A. L. Efros, *Sov. Phys. Semiconduct.*, 1982, **16**, 772–775.
37. J. B. Khurgin, E. W. Forsythe, G. S. Tompa and B. A. Kahn, *Phys. Rev. Lett.*, 1996, **69**, 1241–1243.
38. L. W. Wang and A. Zunger, *J. Chem. Phys.*, 1994, **100**, 2394–2397.
39. S. Goedecker, *Rev. Mod. Phys.*, 1999, **71**, 1085–1123.
40. D. R. Bowler, T. Miyazaki and M. J. Gillan, *J. Phys.: Condens. Matter*, 2002, **14**, 2781–2798.
41. J. M. Soler, E. Artacho, J. D. Gale, A. García, J. Junquera, P. Ordejón and D. Sánchez-Portal, *J. Phys.: Condens. Matter*, 2002, **14**, 2745–2780.
42. C. Ochsenfeld and M. Head-Gordon, *Chem. Phys. Lett.*, 1997, **270**, 399–405.
43. A. M. N. Niklasson and M. Challacombe, *Phys. Rev. Lett.*, 2004, **92**, 193001.
44. S. Coriani, S. Høst, B. Jansik, L. Thøgersen, J. Olsen, P. Jørgensen, S. Reine, F. Pawłowski, T. Helgaker and P. Sałek, *J. Chem. Phys.*, 2007, **126**, 154108.
45. D. Sundholm, *Nano Lett.*, 2003, **3**, 847–849.
46. R. Send and D. Sundholm, *Phys. Chem. Chem. Phys.*, 2007, **9**, 2862–2867.
47. E. Fabiano, F. Della Sala, G. Barbarella, S. Lattante, M. Anni, G. Sotgiu, C. Hättig, R. Cingolani and G. Gigli, *J. Phys. Chem. B*, 2006, **110**, 18651–18660.
48. O. Lehtonen and D. Sundholm, *Phys. Rev. B: Condens. Matter Mater. Phys.*, 2006, **74**, 045433.
49. M. Braskén, M. Lindberg, D. Sundholm and J. Olsen, *Phys. Status Solidi B*, 2000, **221**, 37–41.
50. M. Braskén, M. Lindberg, D. Sundholm and J. Olsen, in *Conference Proceedings Vol. 71: Atoms, Molecules and Quantum Dots* in *Laser Fields: Fundamental Processes*, ed. N Bloembergen, N Rahman and A Rizzo, Societa' Italiana di Fisica, Bologna, 2001, pp. 315–324.
51. M. Braskén, M. Lindberg, D. Sundholm and J. Olsen, *Phys. Status Solidi B*, 2001, **224**, 775–779.
52. M. Braskén, M. Lindberg, D. Sundholm and J. Olsen, *Phys. Rev. B: Condens. Matter Mater. Phys.*, 2001, **64**, 035312.
53. M. Braskén, S. Corni, M. Lindberg, J. Olsen and D. Sundholm, *Mol. Phys.*, 2002, **100**, 911–918.
54. S. Corni, J. Olsen, M. Braskén, M. Lindberg and D. Sundholm, *Phys. Rev. B: Condens. Matter Mater. Phys.*, 2003, **67**, 045313.
55. S. Corni, J. Olsen, M. Braskén, M. Lindberg and D. Sundholm, *Phys. Rev. B: Condens. Matter Mater. Phys.*, 2003, **67**, 085314.
56. S. Corni, M. Braskén, M. Lindberg, J. Olsen and D. Sundholm, *Physica E*, 2003, **18**, 436–442.
57. T. Vänskä, M. Lindberg, J. Olsen and D. Sundholm, *Phys. Status Solidi B*, 2006, **243**, 4035–4045.
58. *QDOT* is a configuration-interaction and coupled-cluster program for semiconductor quantum dots authored by M. Braskén, S. Corni, M. Lindberg, J. Olsen, D. Sundholm and T. Vänskä, 2005.
59. P. Y. Yu and M. Cardona, *Fundamentals of Semiconductors: Physics and Materials Properties*, Springer, 3rd edn, 2005.
60. C. Pickering, M. I. J. Beale, D. J. Robbins, P. J. Pearson and R. Greef, *J. Phys. C: Solid State Phys.*, 1984, **17**, 6535–6552.
61. L. T. Canham, *Appl. Phys. Lett.*, 1990, **57**, 1046–1048.
62. H. Wong, V. Filip, C. K. Wong and P. S. Chung, *Microelectron. Reliab.*, 2007, **47**, 1–10.
63. L. T. Canham, in *Properties of Porous Silicon*, ed. L. T. Canham, Institution of Engineering and Technology, 1997, pp. 249–255.
64. G. Belomoin, J. Terrien, A. Smith, S. Rao, R. Twesten, S. Chaieb, L. Wagner, L. Mitas and M. H. Nayfeh, *Appl. Phys. Lett.*, 2002, **80**, 841–843.
65. Y. Kanemitsu, *Phys. Rep.*, 1995, **263**, 1–91.
66. M. H. Nayfeh and L. Mitas, in *Nanosilicon*, ed. V Kumar, Elsevier, Amsterdam, 2007, pp. 3–78.
67. L. T. Canham, in *Properties of Porous Silicon*, ed. L. T. Canham, INSPEC, The Institution of Electrical Engineers, London, UK, 1997, pp. 247–255.
68. G. Allan, C. Delerue and M. Lannoo, *Phys. Rev. Lett.*, 1996, **76**, 2961–2964.
69. P. Roura and J. Costa, *Eur. J. Phys.*, 2002, **23**, 191–203.
70. D. Kovalev, H. Heckler, G. Polisski and F. Koch, *Phys. Status Solidi B*, 1999, **215**, 871–932.
71. G. M. Credo, M. D. Mason and S. K. Burattoa, *Appl. Phys. Lett.*, 1999, **74**, 1978–1980.
72. O. Lehtonen and D. Sundholm, in *Silicon Nanophotonics: Basic Principles Present Status and Perspectives*, ed. L Khriachtchev, World Scientific, Singapore, 2008.
73. D. Sundholm, *Phys. Chem. Chem. Phys.*, 2004, **6**, 2044–2047.
74. A. Smith, Z. H. Yamani, N. Roberts, J. Turner, S. R. Habbal, S. Granick and M. H. Nayfeh, *Phys. Rev. B: Condens. Matter Mater. Phys.*, 2005, **72**, 205307.
75. C. Marschner, J. Baumgartner and A. Wallner, *Dalton Trans.*, 2006, 5667–5674.
76. D. Jurbergs, E. Rogojina, L. Mangolini and U. Kortshagen, *Appl. Phys. Lett.*, 2006, **88**, 233116.
77. L. Pavesi, L. Dal Negro, C. Mazzoleni, G. Franzó and A. Priolo, *Nature*, 2000, **408**, 440–444.
78. H. Suzuki, S. Hoshino, K. Furukawa, K. Ebata, C. H. Yuan and I. Bleyl, *Polym. Adv. Technol.*, 2000, **11**, 460–467.
79. F. Schauer, I. Kuritka, N. Dokoupil and P. Horváth, *Physica E*, 2002, **14**, 272–276.
80. V. I. Klimov, *J. Phys. Chem. B*, 2000, **104**, 6112–6123.
81. V. I. Klimov, *Annu. Rev. Phys. Chem.*, 2007, **58**, 635–678.
82. G. Bastard, *Wave Mechanics Applied to Semiconductor Heterostructures*, Les Ulis, 1988.
83. M. G. Burt, *J. Phys.: Condens. Matter*, 1999, **11**, R53–R83.
84. O. Stier, M. Grundmann and D. Bimberg, *Phys. Rev. B: Condens. Matter Mater. Phys.*, 1999, **59**, 5688–5701.
85. K. Leung and K. B. Whaley, *Phys. Rev. B: Condens. Matter Mater. Phys.*, 1997, **56**, 7455–7468.
86. T. Takagahara and K. Takeda, *Phys. Rev. B: Condens. Matter Mater. Phys.*, 1996, **53**, R4205–R4208.
87. U. Bockelmann, *Phys. Rev. B: Condens. Matter Mater. Phys.*, 1993, **48**, 17637–17640.
88. H. Koch and P. Jørgensen, *J. Chem. Phys.*, 1990, **93**, 3333–3344.
89. O. Christiansen, H. Koch and P. Jørgensen, *Chem. Phys. Lett.*, 1995, **243**, 409–418.
90. O. Christiansen, H. Koch and P. Jørgensen, *J. Chem. Phys.*, 1995, **103**, 7429–7441.
91. R. H. Haug and S. W. Koch, *Quantum Theory of the Optical and Electronic Properties of Semiconductors*, World Scientific, Singapore, 1990.
92. D. Bimberg, M. Grundmann and N. Ledentsov, *Quantum Dot Heterostructures*, Wiley, New York, 1999.
93. T. Wenckebach, *Essentials of Semiconductor Physics*, Wiley, Chichester, 1999.
94. J. Singh, *Physics of Semiconductors and their Heterostructures*, McGraw-Hill, New York, 1993.
95. P. Å. Malmqvist, *Int. J. Quantum Chem.*, 1986, **30**, 479–494.
96. J. Olsen, M. R. Godefroid, P. Jönsson, P. Å. Malmqvist and C. F. Fischer, *Phys. Rev. E*, 1995, **52**, 4499–4508.
97. T. Helgaker, P. Jørgensen and J. Olsen, *Molecular Electronic-Structure Theory*, Wiley, Chichester, 2000.
98. R. Ahlrichs, M. Bär, M. Häser, H. Horn and C. Kölmel, *Chem. Phys. Lett.*, 1989, **162**, 165–169.
99. P. Hohenberg and W. Kohn, *Phys. Rev. Sect. B*, 1964, **136**, 864–871.
100. W. Kohn and L. J. Sham, *Phys. Rev. Sect. A*, 1965, **140**, 1133–1138.
101. E. Runge and E. K. U. Gross, *Phys. Rev. Lett.*, 1984, **52**, 997–1000.
102. K. Burke, J. Werschnick and E. K. U. Gross, *J. Chem. Phys.*, 2005, **123**, 062206.
103. R. van Leeuwen, *Int. J. Mod. Phys. B*, 2001, **15**, 1969–2023.
104. O. Lehtonen and D. Sundholm, *J. Chem. Phys.*, 2006, **125**, 144314.
105. K. Eichkorn, O. Treutler, H. Öhm, M. Häser and R. Ahlrichs, *Chem. Phys. Lett.*, 1995, **242**, 652–660.
106. K. Eichkorn, F. Weigend, O. Treutler and R. Ahlrichs, *Theor. Chem. Acc.*, 1997, **97**, 119–124.
107. R. Bauernschmitt, M. Häser, O. Treutler and R. Ahlrichs, *Chem. Phys. Lett.*, 1997, **264**, 573–578.

108. P. Deglmann, K. May, F. Furche and R. Ahlrichs, *Chem. Phys. Lett.*, 2004, **384**, 103–107.
109. A. Köhn and C. Hättig, *J. Chem. Phys.*, 2003, **119**, 5021–5036.
110. C. Hättig, *Adv. Quantum Chem.*, 2005, **50**, 37–60.
111. U. Itoh, Y. Yasutake, H. Onuki, N. Washida and T. Ibuki, *J. Chem. Phys.*, 1986, **85**, 4867–4872.
112. F. Fehér, *Molekülspektroskopische Untersuchungen auf dem Gebiet der Silane und der Heterocyclischen Sulfane*, Forschungsbericht des Landes Nordrhein-Westfalen, Westdeutscher Verlag, Köln, 1977.
113. T. H. Dunning, Jr, K. A. Peterson and A. K. Wilson, *J. Chem. Phys.*, 2001, **114**, 9244–9253.
114. J. P. Perdew, K. Burke and M. Ernzerhof, *J. Chem. Phys.*, 1996, **105**, 9982–9985.
115. A. D. Becke, *J. Chem. Phys.*, 1993, **98**, 5648–5652.
116. C. Lee, W. Yang and R. G. Parr, *Phys. Rev. B: Condens. Matter Mater. Phys.*, 1988, **37**, 785–789.
117. J. Fischer, J. Baumgartner and C. Marschner, *Science*, 2005, **310**, 825–825.
118. A. Schäfer, H. Horn and R. Ahlrichs, *J. Chem. Phys.*, 1992, **97**, 2571–2577.
119. A. Schäfer, C. Huber and R. Ahlrichs, *J. Chem. Phys.*, 1994, **100**, 5829–5835.
120. F. Weigend and R. Ahlrichs, *Phys. Chem. Chem. Phys.*, 2005, **7**, 3297–3305.
121. D. E. Woon and T. H. Dunning, Jr, *J. Chem. Phys.*, 1993, **98**, 1358–1371.
122. F. Weigend, F. Furche and R. Ahlrichs, *J. Chem. Phys.*, 2003, **119**, 12753–12762.
123. S. H. Vosko, L. Wilk and M. Nusair, *Can. J. Physs*, 1980, **58**, 1200–1211.
124. J. P. Perdew, *Phys. Rev. B: Condens. Matter Mater. Phys.*, 1986, **33**, 8822–8824.
125. A. D. Becke, *Phys. Rev. A: At., Mol., Opt. Phys.*, 1988, **38**, 3098–3100.
126. M. Rohlfing and S. G. Louie, *Phys. Rev. Lett.*, 1998, **80**, 3320–3323.
127. J. C. Grossman, M. Rohlfing, L. Mitas, S. G. Louie and M. L. Cohen, *Phys. Rev. Lett.*, 2001, **86**, 472–475.
128. L. X. Benedict, A. Puzder, A. J. Williamson, J. C. Grossman, G. Galli, J. E. Klepeis, J. Y. Raty and O. Pankratov, *Phys. Rev. B: Condens. Matter Mater. Phys.*, 2003, **68**, 085310.
129. A. R. Porter, M. D. Towler and R. J. Needs, *Phys. Rev. B: Condens. Matter Mater. Phys.*, 2001, **64**, 035320.
130. J. E. Vincent, J. Kim and R. M. Martin, *Phys. Rev. B: Condens. Matter Mater. Phys.*, 2007, **75**, 045302.
131. J. C. Grossman, *J. Chem. Phys.*, 2002, **117**, 1434–1440.
132. A. J. Williamson, R. Q. Hood and J. C. Grossman, *Phys. Rev. Lett.*, 2001, **87**, 246406.
133. C. Delerue, G. Allan and M. Lannoo, *Phys. Rev. B: Condens. Matter Mater. Phys.*, 1993, **48**, 11024–11036.
134. C. Meier, A. Gondorf, S. Lüttjohann and A. Lorke, *J. Appl. Phys.*, 2007, **101**, 103112.
135. S. Rao, K. Mantey, J. Therrien, A. Smith and M. H. Nayfeh, *Phys. Rev. B: Condens. Matter Mater. Phys.*, 2007, **79**, 155316.
136. A. Franceschetti and S. T. Pantelides, *Phys. Rev. B: Condens. Matter Mater. Phys.*, 2003, **68**, 033313.
137. M. H. Nayfeh, N. Rigakis and Z. Yamani, *Phys. Rev. B: Condens. Matter Mater. Phys.*, 1997, **56**, 2079–2084.
138. M. H. Nayfeh, O. Akcakir, J. Terrien, Z. Yamani, N. Barry, W. Yu and E. Gratton, *Appl. Phys. Lett.*, 1999, **75**, 4112–4114.
139. O. Akcakir, J. Terrien, G. Belomoin, N. Barry, J. D. Muller, E. Gratton and M. H. Nayfeh, *Appl. Phys. Lett.*, 2000, **76**, 1857–1859.
140. M. H. Nayfeh, N. Barry, J. Terrien, O. Akcakir, E. Gratton and G. Belomoin, *Appl. Phys. Lett.*, 2001, **78**, 1131–1133.
141. X. Zhang, D. Neiner, A. Wang, A. Y. Louie and S. M. Kauzlarich, *Nanotechnology*, 2007, **18**, 095601.
142. M. H. Nayfeh, O. Akcakir, G. Belomoin, N. Barry, J. Therrien and E. Gratton, *Appl. Phys. Lett.*, 2000, **77**, 4086–4088.
143. C. S. Garoufalis, A. D. Zdetsis and S. Grimme, *Phys. Rev. Lett.*, 2001, **87**, 276402.
144. L. Mitas, J. Terrien, R. Twesten, G. Belomoin and M. H. Nayfeh, *Appl. Phys. Lett.*, 2001, **78**, 1918–1920.
145. M. H. Nayfeh, in *Conference Proceedings, vol. 71: Atoms Molecules and Quantum Dots in Laser Fields: Fundamental Processes*, ed. N Bloembergen, N Rahman and A Rizzo, Societa' Italiana di Fisica, Bologna, 2001, pp. 83–96.
146. G. Belomoin, E. Rogozhina, J. Terrien, P. V. Braun, L. Abuhassan, M. H. Nayfeh, L. Wagner and L. Mitas, *Phys. Rev. B: Condens. Matter Mater. Phys.*, 2002, **65**, 193406.
147. I. Vasiliev, S. Ogut and J. R. Chelikowsky, *Phys. Rev. B: Condens. Matter Mater. Phys.*, 2002, **65**, 115416.
148. E. W. Draeger, J. C. Grossman, A. J. Williamson and G. Galli, *Phys. Rev. Lett.*, 2003, **90**, 167402.
149. A. Puzder, A. J. Williamson, J. C. Grossman and G. Galli, *J. Am. Chem. Soc.*, 2003, **125**, 2786–2791.
150. Z. Zhou, R. A. Friesner and L. Brus, *J. Am. Chem. Soc.*, 2003, **125**, 15599–15607.
151. Z. Zhou, L. Brus and R. A. Friesner, *Nano Lett.*, 2003, **3**, 163–167.
152. E. Degoli, G. Cantele, E. Luppi, R. Magri, D. Ninno, O. Bisi and S. Ossicini, *Phys. Rev. B: Condens. Matter Mater.Phys.*, 2004, **69**, 155411.
153. E. Luppi, E. Degoli, G. Cantele, S. Ossicini, R. Magri, D. Ninno, O. Bisi, O. Pulci, G. Onida, M. Gatti, A. Incze and R. Del Sole, *Opt. Mater.*, 2004, **27**, 1008–1013.
154. S. Rao, J. Sutin, R. Clegg, E. Gratton, M. H. Nayfeh, S. Habbal, A. Tsolakidis and R. M. Martin, *Phys. Rev. B: Condens. Matter Mater. Phys.*, 2004, **69**, 205319.
155. Y. B. Ge and J. D. Head, *Mol. Phys.*, 2005, **103**, 1035–1045.
156. F. A. Reboredo and G. Galli, *J. Phys. Chem. B*, 2005, **109**, 1072–1078.
157. C. S. Garoufalis and A. D. Zdetsis, *Phys. Chem. Chem. Phys.*, 2006, **8**, 808–813.
158. O. Lehtonen and D. Sundholm, *Phys. Chem. Chem. Phys.*, 2006, **8**, 4228–4232.
159. F. Pichierri, *Chem. Phys. Lett.*, 2006, **421**, 319–323.
160. B. Delley and E. F. Steigmeier, *Phys. Rev. B: Condens. Matter Mater. Phys.*, 1993, **47**, 1397–1400.
161. D. A. Eckhoff, J. D. B. Sutin, R. M. Clegg, E. Gratton, E. V. Rogozhina and P. V. Braun, *J. Phys. Chem. B*, 2005, **109**, 19786–19797.
162. I. Vasiliev, J. R. Chelikowsky and R. M. Martin, *Phys. Rev. B: Condens. Matter Mater. Phys.*, 2002, **65**, 121302.
163. M. V. Wolkin, J. Jorne, P. M. Fauchet, G. Allan and C. Delerue, *Phys. Rev. Lett.*, 1999, **82**, 197–200.
164. X. D. Pi, L. Mangolini, S. A. Campbell and U. Kortshagen, *Phys. Rev. B: Condens. Matter Mater. Phys.*, 2007, **75**, 085423.
165. Y. Takeda, S. Hyodo, N. Suzuki, T. Motohiro, T. Hioki and S. Noda, *J. Appl. Phys.*, 1993, **73**, 1924–1928.
166. K. Luterová, I. Pelant, P. Fojtík, M. Nikl, I. Gregora, J. Kočka, J. Dian, J. Valenta, P. Malý, J. Kudrna, J. Štepánek, A. Poruba and P. Horváth, *Philos. Mag. B*, 2000, **80**, 1811–1832.
167. K. Luterová, A. Poruba, J. Dian, O. Salyk, P. Horváth, P. Knápek, J. Valenta, J. Kočka and I. Pelant, *J. Porous Mater.*, 2000, **7**, 135–138.
168. J. Mu, L. Xu, X. Gao and Y. Zhang, *J. Dispersion Sci. Technol.*, 2005, **26**, 483–486.
169. M. D. Mason, D. J. Sirbuly, P. J. Carson and S. K. Burattoa, *J. Chem. Phys.*, 2001, **114**, 8119–8123.